



(12) **EUROPEAN PATENT SPECIFICATION**

(45) Date of publication and mention  
of the grant of the patent:  
**27.12.2000 Bulletin 2000/52**

(21) Application number: **92906273.5**

(22) Date of filing: **17.01.1992**

(51) Int. Cl.<sup>7</sup>: **G01N 21/65, A61B 5/00**

(86) International application number:  
**PCT/US92/00420**

(87) International publication number:  
**WO 92/15008 (03.09.1992 Gazette 1992/23)**

(54) **SYSTEMS AND METHODS OF MOLECULAR SPECTROSCOPY TO PROVIDE FOR THE  
DIAGNOSIS OF TISSUE**

MOLEKULARSPEKTROSKOPIEVERFAHREN UND -EINRICHTUNGEN ZUR GEWEBEDIAGNOSE  
SYSTEMES ET PROCEDES DE SPECTROSCOPIE MOLECULAIRE, PERMETTANT D'ETABLIR LE  
DIAGNOSTIC DES TISSUS

(84) Designated Contracting States:  
**AT BE CH DE DK ES FR GB GR IT LI LU MC NL  
SE**

(30) Priority: **26.02.1991 US 661077**

(43) Date of publication of application:  
**15.12.1993 Bulletin 1993/50**

(73) Proprietor:  
**MASSACHUSETTS INSTITUTE OF  
TECHNOLOGY  
Cambridge, MA 02139 (US)**

(72) Inventors:  
• **RAVA, Richard, P.**  
**Waltham, MA 02154 (US)**  
• **BARAGA, Joseph, J.**  
**Somerville, MA 02143 (US)**  
• **FELD, Michael, S.**  
**Waban, MA 02168 (US)**

(74) Representative:  
**Harvey, David Gareth**  
**Graham Watt & Co.**  
**Riverhead**  
**Sevenoaks Kent TN13 2BN (GB)**

(56) References cited:  
**WO-A-90/06718 US-A- 4 758 081**

- **APPLIED SPECTROSCOPY** vol. 43, no. 3, 1 March 1989, pages 372 - 375; J. WILLIAMSON ET AL.: 'NEAR INFRARED RAMAN SPECTROSCOPY,ETC.'
- **APPLIED SPECTROSCOPY REVIEWS** vol. 24, no. 3, 1 July 1988, pages 259 - 312; Y. OZAKI: 'MEDICAL APPLICATION OF RAMAN SPECTROSCOPY'
- **APPLIED SPECTROSCOPY** vol. 42, no. 7, 1 July 1988, pages 1188 - 1193; E.N.LEWIS ET AL.: 'DEVELOPMENT OF NEAR INFRARED FOURIER TRANSFORM RAMAN SPECTROSCOPY,ETC.'
- **ANALYTICAL CHEMISTRY** vol. 56, no. 12, 1 October 1984, pages 2199 - 2204; S. SCHWAB ET AL.: 'VERSATILE EFFICIENT RAMAN SAMPLING,ETC.'
- **APPLIED OPTICS** vol. 30, no. 1, 1 January 1991, pages 98 - 105; K.ONO ET AL.: 'FIBER OPTIC REFLECTANCE SPECTROPHOTOMETRY SYSTEM,ETC.'
- **SPECTROSCOPY**, vol.5, no.24, 1990, page - , NIE ET ALL 'APPLICATIONS OF NEAR-INFRARED FOURIER TRANSFORM RAMAN SPECTROSCOPY IN BIOLOGY AND MEDICINE'

Note: Within nine months from the publication of the mention of the grant of the European patent, any person may give notice to the European Patent Office of opposition to the European patent granted. Notice of opposition shall be filed in a written reasoned statement. It shall not be deemed to have been filed until the opposition fee has been paid. (Art. 99(1) European Patent Convention).

## Description

[0001] In the United States heart attacks, almost entirely attributable to coronary atherosclerosis, account for 20-25% of all deaths. Several medical and surgical therapies are available for treatment of atherosclerosis; however, at present no *in situ* methods exist to provide information in advance as to which lesions will progress despite a particular medical therapy.

[0002] Objective clinical assessments of atherosclerotic vessels are at present furnished almost exclusively by angiography, which provides anatomical information regarding plaque size and shape as well the degree of vessel stenosis. The decision of whether an interventional procedure is necessary and the choice of appropriate treatment modality is usually based on this information. However, the histological and biochemical composition of atherosclerotic plaques vary considerably, depending on the stage of the plaque and perhaps also reflecting the presence of multiple etiologies. This variation may influence both the prognosis of a given lesion as well as the success of a given treatment. Such data, if available, might significantly assist in the proper clinical management of atherosclerotic plaques, as well as in the development of a basic understanding of the pathogenesis of atherosclerosis.

[0003] At present biochemical and histological data regarding plaque composition can only be obtained either after treatment, by analyzing removed material, or at autopsy. Plaque biopsy is contraindicated due to the attendant risks involved in removing sufficient arterial tissue for laboratory analysis. Recognizing this limitation, a number of researchers have investigated optical spectroscopic methods as a means of assessing plaque deposits. Such "optical biopsies" are non-destructive, as they do not require removal of tissue, and can be performed rapidly with optical fibers and arterial catheters. With these methods, the clinician can obtain, with little additional risk to the patient, information that is necessary to predict which lesions may progress and to select the best treatment for a given lesion.

[0004] Among optical methods, most attention has centered on ultraviolet and/or visible fluorescence. Fluorescence spectroscopy has been utilized to diagnose disease in a number of human tissues, including arterial wall. In arterial wall, fluorescence of the tissue has provided for the characterization of normal and atherosclerotic artery. However the information provided is limited by the broad line width of fluorescence emission signals. Furthermore, for the most part, fluorescence based methods provide information about the electronic structure of the constituent molecules of the sample. There is a need for non-destructive real time biopsy methods which provide more complete and accurate biochemical and molecular diagnostic information. This is true for atherosclerosis as well as other diseases which affect the other organs of the body.

[0005] An article titled "Applications of Near-Infrared Fourier Transform Raman Spectroscopy in Biology and Medicine", in *Spectroscopy*, vol. 5 No. 24 (1990) by Nie, *et al.* discloses a spectroscopic diagnostic system and a method of spectroscopic analysis according to the preambles of claims 1 and 5, respectively.

[0006] An article titled "Medical Application of Raman Spectroscopy", in *Applied Spectroscopy Reviews*, 24 (3 and 4), 259-312 (1988) by Ozaki states that "in order to measure the Raman spectra of the cells, tissues, and organs satisfactorily, however, two major problems must be circumvented. These are fluorescence from samples and/or impurities which intrinsically mask weaker Raman scattering and damage to samples by strong laser illumination. Biological materials, especially morbid ones, often emit strong fluorescence. Therefore, the solution to the fluorescence problem is the key to making great strides in the Raman study of biomedical materials. The best solution to elimination of the fluorescence of biomedical materials is probably to change the excitation wavelength further into the red. In this respect the development of detectors with high-sensitivity in the red and progress in near-infrared Raman spectroscopy (89) and Fourier-transform Raman spectroscopy [90, 91] are very much to be desired".

[0007] An article titled "Near-Infrared Raman Spectroscopy with a 783-nm Diode Laser and CCD Array Detector", in *Applied Spectroscopy* 43 (1989) January, No.1, by Williamson, *et al.* discloses an apparatus comprising a GaAlAs diode laser operating at 783 nm combined with an unintensified charge coupled device (CCD) array detector and a single grating spectrograph and used to obtain near-infrared (NIR) Raman spectra. The article opines that the laser diode/CCD system represents a compromise which should have reduced fluorescence rejection, compared to FT-Raman with 1064 nm excitation, but should permit major gains in sensitivity and simplicity.

[0008] The system and method of the present invention is characterised by the features of the characterising portions of claims 1 and 5, respectively.

[0009] The present invention relates to vibrational spectroscopic systems for, and methods of, near-infrared (IR) FT-Raman spectroscopy which can provide extensive molecular level information about the pathogenesis of disease. This vibrational technique is readily carried out remotely using fiber optic probes. In particular, a preferred embodiment utilizes FT-Raman spectra of human artery for distinguishing normal and atherosclerotic tissue. Near IR FT-Raman spectroscopy can provide information about the tissue state which is unavailable from fluorescence methods. *In situ* vibrational spectroscopic techniques allow probing of the molecular level changes taking place during disease progression. The information provided is used to guide the choice of the correct treatment modality.

[0010] These methods include the steps of irradiating the tissue to be diagnosed with radiation in the infrared range of the electromagnetic spectrum, detecting light emitted by the tissue at the same frequency, or alternatively, within a

range of frequencies on one or both sides of the irradiating light, and analyzing the detected light to diagnose its condition. The Raman method is based on the acquisition of information about molecular vibrations which occur in the range of wavelengths between 3 and 300 microns. Note that with respect to the use of Raman shifted light, excitation wavelengths in the ultraviolet, visible and infrared ranges can all produce diagnostically useful information. Near IR FT-Raman spectroscopy is ideally suited to the study of human tissue.

**[0011]** Raman spectroscopy is an important method in the study of biological samples, in general because of the ability of this method to obtain vibrational spectroscopic information from any sample state (gas, liquid or solid) and the weak interference from the water Raman signal in the "fingerprint" spectral region. The FT-spectrometer furnishes high throughput and wavelength accuracy which might be needed to obtain signals from tissue and measure small frequency shifts that are taking place. Finally, standard quartz optical fibers can be used to excite and collect signals remotely.

**[0012]** Near IR FT-Raman spectroscopy provides the capability to probe biological constituents many hundred microns below the tissue surface. In particular, for atherosclerotic tissue, calcified deposits below the tissue surface are easily discerned. Thus, it becomes possible to detect pathologic conditions which would not be apparent using angiographic methods, as well as to study the detailed molecular basis of the pathology.

**[0013]** In contrast with electronic techniques, the bands in a vibrational spectrum are relatively narrow and easy to resolve. Vibrational bands are readily assigned to individual molecular groups.

**[0014]** Another preferred embodiment of the present invention uses two or more diagnostic procedures either simultaneously or sequentially collected to provide for a more complete diagnosis. These methods can include the use of fluorescence of endogenous tissue, Raman shifted measurements and/or ATR measurements.

**[0015]** One particular embodiment of the present invention employs laser light in the 810 nm range to illuminate the tissue and thereby provide Raman spectra having frequency components in a range suitable for detection by the CCD. Other wavelengths can be employed to optimize the diagnostic information depending upon the particular type of tissue and the type and stage of disease or abnormality. Raman spectra can be collected by the CCD at two slightly different illumination frequencies and are subtracted from one another to remove broadband fluorescence light components and thereby produce a high quality Raman spectrum. The high sensitivity of the CCD detector combined with the spectra subtraction technique allow high quality Raman spectra to be produced in less than 1 second with laser illumination intensity similar to that for the FT-Raman system also described herein.

Figures 1A and 1C are schematic illustrations of systems which are not according to the present invention but useful in understanding the present invention. Figure 1B is a axial cross-section view of a catheter useful with the present invention.

Figure 2 graphically illustrates FT-Raman spectra of human aorta: a) normal artery; b) atheromatous plaque; c) FT-Raman spectrum solid cholesterol (Sigma).

Figure 3 graphically illustrates FT-Raman spectra of normal human aorta: a) irradiated from intimal side (spectrum multiplied by 3); and b) irradiated from adventitial side (primary adipose tissue). c) NIR FT-Raman spectrum of triglyceride, triolein.

Figure 4 graphically illustrates FT-Raman spectra from human aorta: a) fibrous plaque; and b) atheromatous plaque. c) FT-Raman spectrum of cholesterol monohydrate powder.

Figure 5 graphically illustrates FT-Raman spectra of calcified human aorta: a) calcified with fibrous cap; b) excised calcification from a different plaque; c) spectra of the same tissue as in a) taken from adventitial side.

Figure 6 graphically illustrates FT-Raman spectra of calcified human aorta: a) calcified plaque with a fibrous cap (spectrum multiplied by 8); and b) exposed calcification.

Figure 7 graphically illustrates the measured NIR Raman intensity of the  $960\text{ cm}^{-1}$  band ( $A(960\text{ cm}^{-1})$  indicates the area of this band) in a calcified deposit as a function of depth below the irradiated surface. The dashed curve corresponds to the fit of an exponential function to the data with an exponent of  $2.94\text{ mm}^{-1}$ .

Figure 8 graphically illustrates FT-IR ATR spectra ( $4000 - 700\text{ cm}^{-1}$ ) of (a) normal aorta, intimal surface; and (b) buffered saline (0.14M NaCl, pH 7.4).

Figure 9 graphically illustrates FT-IR ATR spectra ( $1800 - 800\text{ cm}^{-1}$ ) after water subtraction: (a) Normal aorta, intimal surface; (b) Sub-adventitial fat; (c) Saline rinsed from the intimal surface of normal aorta.

Figure 10 graphically illustrates FT-IR ATR spectra ( $1800 - 800\text{ cm}^{-1}$ ): (a) Two consecutive water-subtracted spectra of normal aorta, intimal surface, collected immediately after placement on ATR element (solid line) and 10 minutes later (dashed line); (b) Same two spectra as in (a) after lipid subtraction, scaled to have equal maxima.

Figure 11 graphically illustrates FT-IR ATR spectra ( $1800 - 800\text{ cm}^{-1}$ ), water-and lipid-subtracted: (a) Normal aorta, media layer; (b) Atherosclerotic plaque, intimal surface; (c) Atheromatous plaque with intact fibrous cap, intimal surface.

Figure 12 graphically illustrates FT-IR ATR spectra ( $1800 - 800\text{ cm}^{-1}$ ): (a) Necrotic core of atheromatous plaque, water-and lipid-subtracted; (b) Dry film of cholesterol.

Figure 13 graphically illustrates scatter plot for all samples of the area,  $A(1050)$ , of the  $1050\text{ cm}^{-1}$  cholesterol band (integrated from  $1075$  to  $1000\text{ cm}^{-1}$ ) ratioed to the area,  $A(1550)$  of the  $1548\text{ cm}^{-1}$  protein amide II band (integrated from  $1593$  to  $1485\text{ cm}^{-1}$ ). The intensities were calculated from the water-and lipid-subtracted spectra. NORMAL denotes normal aorta specimens, intimal side, FIBROUS includes atherosclerotic and atheromatous plaques with intact fibrous caps, and NECROTIC includes exposed necrotic atheroma cores and necrotic material isolated from atheromatous plaques.

Figure 14 graphically illustrates FT-IR ATR spectra ( $1800 - 800\text{ cm}^{-1}$ ): (a) Second derivative spectrum of normal aorta intima (Figure 8a); (b) Water-subtracted spectrum of same normal aorta intima specimen (same as Figure 9a).

Figure 15 graphically illustrates a scatter diagram for all the specimens of the area,  $A(1050)$  of the  $1050\text{ cm}^{-1}$  cholesterol band plotted versus the area,  $A(1382)$ , of the  $1382\text{ cm}^{-1}$  cholesterol band. Both cholesterol bands have been normalized to the area,  $A(1050)$ , of the protein amide II band. All band intensities were calculated from the water-and lipid-subtracted spectra. Tissue categories are the same as in Figure 13. The solid line represents a linear least squares fit to the data.

Figures 16A and 16B are additional embodiments of ATR probes again not according to the present invention.

Figure 17 is a schematic diagram of the system of Figure 1A modified to use the spectrograph and CCD Raman detector of the present invention.

Figure 18 is a schematic diagram of a preferred system for implementing the spectrograph and CCD Raman detector of the present invention.

Figure 19 graphically illustrates spectrograph and CCD-Raman spectra of normal human aorta: A) Raman plus fluorescence spectrum produced by illuminating the tissue sample with  $810\text{ nm}$  laser light; B) Raman difference spectrum produced by subtracting spectra produced by illuminating the tissue sample with  $810$  and  $812\text{ nm}$  laser light; C) resulting Raman spectrum produced by integrating the Raman difference spectrum of B).

Figure 20 graphically illustrates spectrograph and CCD-Raman spectra of an atherosclerotic plaque with a calcified deposit exposed at the surface: A) Raman plus fluorescence spectrum produced by illuminating the tissue sample with  $810\text{ nm}$  laser light; B) Raman difference spectrum produced by subtracting spectra produced by illuminating the tissue sample with  $810$  and  $812\text{ nm}$  laser light; C) resulting Raman spectrum produced by integrating the Raman difference spectrum of B).

Figure 21 graphically illustrates a spectrograph/CCD-Raman spectrum of adventitial adipose tissue.

**[0016]** The spectroscopic methods which are not according to the present invention can be performed on a system such as that for laser treatment of atherosclerosis which is illustrated in Figure 1A. Figure 1A includes separate block diagrams for the system of the invention which utilizes laser light for spectroscopic diagnosis as well as for treatment and/or removal of tissue. The ablation laser 225, pulse stretcher 229 and the pulse filler/multiplexer 231, 233 produce an output laser ablation pulse of sufficient energy and intensity to remove tissue and sufficient pulse duration to propagate through a fiber optic laser catheter delivery system without damaging the fibers. These systems and methods are more fully described in co-pending application U.S. Serial No. 07/644,202 filed on January 22, 1991.

**[0017]** To remove plaque, a device 219 is used to contact the tissue such as multiple-fiber laser catheter 10 of Figure 1B with an optical shield. The catheter 10 is inserted into the artery and the distal end of the catheter is brought into contact with the lesion. Next, a determination is made as to the type of tissue at which each optical fiber 20a-c' is aimed. Only fibers aimed at diseased tissue are activated. Thus, selective tissue removal is obtained. Furthermore, this technique is also applicable for guiding surgical procedures in other organs and tissue types such as the colon and bladder.

**[0018]** The present invention relates to systems and methods of performing spectral diagnostics to diagnose the tissue in front of each fiber. In a preferred arrangement a laser light source 207 that is coupled to the fibers. The diagnostic light is sent to the fiber of choice by the optical fiber selector 217.

**[0019]** The diagnostic light exits the selected optical fiber and falls on the tissue. The tissue absorbs the light and a fraction of the absorbed light is re-emitted, by Rayleigh fluorescence, Raman or other elastic or inelastic light scattering processes. This light is returned to the optical fibers and exits from selector 217, and is detected by a photodiode, photomultiplier or other detector 203. Returning light could use different optical fibers than those employed for illumination. Diagnostic subsystem produces the entire spectral signal which is coupled to computer 80.

**[0020]** The computer stores the information in a memory as a spectrum, which is a graph of light intensity vs. wavelength. This can be displayed immediately on the video display 82 or compared to an existing spectrum stored in the computer and the difference displayed on the spectral display 86. Temporal display 88 can display corrections made for the wavelength dependent sensitivities of the source. Information from either the temporal or spectral display can be stored in the computer 80. The comparative data is shown on numerical display 84 to provide a quantitative measure of the health of the tissue observed.

**[0021]** With a multichannel detector and a computer, or with appropriate multiple filters and detectors, it is possible to gather this information in a fraction of a second. Thus, a spectral or numerical display is provided which indicates the

type of tissue at which the fiber of interest is aimed. If the tissue is plaque, and is to be removed, then fiber selector 217 will align this fiber with the output beam of the high power laser 225. Then, the high power laser 225 is turned on and an appropriate power level is selected for a predetermined amount of time to remove a certain amount of diseased tissue. The beam of laser 225 is transmitted to pulse stretcher 229 and pulse filler/multiplexer 231, 233 to properly adjust the beam fluence.

**[0022]** The procedure is repeated for different fibers. Where diseased tissue is detected, it is quickly removed. The laser catheter 10 nibbles away at the plaque, leaving the healthy artery wall intact.

**[0023]** If the artery 30 makes a bend 31 as shown by Figure 1B, the laser catheter 10 will tend to make contact with artery wall 32 at the outside wall of the bend. To prevent the catheter from contacting the artery wall, the optical fiber 20c is not fired. The lesion is removed asymmetrically. This allows the laser catheter 10 to follow the lumen 39, 39a around the bend. Thus, the artery wall 32 is not irradiated and is not perforated. Additional details of this fiber optic catheter 10 are disclosed in U.S. Patent No. 4,913,142.

**[0024]** In both Raman and ATR methods, information is contained in the spectral lines which are observed in their intensities, and also their linewidths and center frequencies (and how they change in different environments). Further, Raman and infrared ATR have different "selection rules". Some vibrations seen in infrared won't show up in Raman, and *vice versa*. In other cases the same vibration can be detected by both techniques, but with different relative intensities (e.g. a strong Raman line will be weak in ATR). So in this sense the two techniques provide complementary information and combining the two techniques (or using either or both with laser induced fluorescence) is valuable in diagnosing

**[0025]** The methods can utilize Fourier transform detection to observe the radiation thereby providing improved signal/noise ratios. Other techniques (e.g. diode array detection and CCD detection) can also be used.

**[0026]** As described in more detail below contributions from major tissue constituents can be "subtracted out" to reveal information about molecules which are present in small concentrations. For example, in ATR water contributions are removed before the "dry" tissue constituents could be studied. Also, derivative spectroscopy is used to eliminate background signals and low frequency filters. Note that these techniques deconvolute the observed spectra into its individual constituents, an essential step for optimal extraction of diagnostic information.

**[0027]** While Raman can sample deeply into tissue, ATR samples only a very thin layer (a few microns). Thus, ATR is "naturally" suited to probe surface disease, such as the superficial cancers of the bladder and GI tract, whereas Raman is well suited to providing information about conditions deep inside tissue (such as breast cancer or stones). This is important for 3D imaging. Furthermore, the ATR tissue sampling depth can be controlled by properly matching the probe surface material to the tissue type.

**[0028]** Generally, the ATR signal is very sensitive to the surface of the waveguide or probe. For example, if the probe surface has an affinity for lipids in the tissue, lipids can migrate to the probe surface, creating a thin lipid layer and producing a large signal. This can be a problem (it can give misleading information if not properly recognized and guarded against). Conversely, it can be used to advantage: Probes with special surfaces can be developed to prevent this effect or to promote it, in order to search for particular substances in the tissue.

**[0029]** In a preferred method one can adjust depth probed by ATR by varying refractive index of ATR probe. Alternatively as discussed below one can use a "waveguide needle" to get subsurface information.

**[0030]** Raman diagnostic methods permit adjustment of Raman depth by varying the wavelength. Penetration depth is wavelength dependent, and can be varied by choosing different excitation wavelengths between about  $\lambda=700\text{nm}$  and  $2\mu\text{m}$ . Another potentially important way of adjusting Raman depth is to vary the collection angle. In the near IR, incident (exciting) light is strongly scattered out of the forward direction into larger angles, so Raman signals sampled at smaller angles come from tissue closer to the surface. Therefore, the Raman sampling depth can be controlled to a large extent by probe design.

**[0031]** Depth information is important if one desires to provide imaging by creating 3D images of small tumors in the brain or breast. Differential techniques based on the ideas of the preceding paragraph might allow accurate localization of such tumors in three dimensions. Near-IR Raman can be combined with a sound wave technique (time of flight or standing waves set up in the tissue)--the sound wave would modulate the Raman signal emanating from a point in the tissue when it passes that point, and the modulated signal could be used to establish the depth of the tissue producing the signal.

**[0032]** A system employed for the collection of Raman spectral data from excised tissue samples is illustrated in Figure 1C. FT-Raman spectra were measured from 0 -  $4000\text{cm}^{-1}$  below the laser excitation frequency with a FT-IR interferometer 40 equipped with a FT-Raman accessory. The accessory employed at 180 back scattering geometry and a cooled (77K) InGaAs detector 42.

**[0033]** A 1064 nm CW Nd:YAG laser 44 can be used for irradiating a sample 46: utilizing 500 mW to 1 W laser power in a 1.0 to 2.5 mm spot 48 at the sample 46 to collect Raman data. Alternatively, a pulsed laser source can also be employed. Laser 44 generated a beam 46 that is directed through plasma filter 48, mirrors 50, 52, focussing lens 54 and mirror or prism 56 before irradiating the sample 46. The radiation received by sample 46 undergoes various mechanisms of absorption, reflection and scattering including Raman scattering. Some of the light emitted by the tissue is

directed toward lens 60 and then through one or more Rayleigh filters 62. The collecting lens 60 collects this backscattered light 64 and collimates it. The Rayleigh filters 62 removes the elastically scattered light and transmits the inelastically scattered, frequency shifted (Raman) light. The Raman scattered light enters the interferometer 40. No visible sample degradation was observed under these conditions.

**[0034]** Excised human aorta was chosen of atherosclerotic artery tissue. Samples were obtained at the time of post mortem examination, rinsed with isotonic saline solution (buffered at pH 7.4), snap-frozen in liquid nitrogen, and stored at -85°C until use. Prior to spectroscopic study, samples were passively warmed to room temperature and were kept moist with the isotonic saline. Normal and atherosclerotic areas of tissue were identified by gross inspection, separated, and sliced into roughly 8x8 mm pieces.

**[0035]** The tissue samples were placed in a suprasil quartz cuvette with a small amount of isotonic saline to keep the tissue moist, with one surface in contact with the irradiated by the laser 44. The spectra shown in Figures 2 through 6 were collected with 512 scans at 8 cm<sup>-1</sup> resolution (approximately 35 minutes total collection time).

**[0036]** Human aorta is composed of three distinct layers: intima, media, and adventitia. The intima, normally less than 300 μm thick, is the innermost layer and provides a non-thrombogenic surface for blood flow. It is mainly composed of collagen fibers and ground substance. The medial layer, typically about 500 μm thick, is quite elastic and serves to smooth the pulsatile blood flow from the heart. The structural protein elastin is the major component of aortic media, with some smooth muscle cells present as well. The outermost adventitial layer serves as a connective tissue network which loosely anchors the vessel in place, and is mainly made up of lipids, lipoproteins and collagen. During the atherosclerotic process, the intima thickens due to collagen proliferation, fatty necrotic deposits accumulate under and within the collagenous intima, and eventually, calcium builds up, leading to calcium hydroxyapatite deposits in the artery wall.

**[0037]** Figure 2a shows the FT-Raman spectrum of a full thickness section of aorta grossly identified as normal. Laser irradiation was on the intimal side. The dominant bands appear at 1669 cm<sup>-1</sup> and 1452 cm<sup>-1</sup> and can be assigned to an amide I backbone and C-H in-plane bending vibration from proteins, respectively. Weaker bands at 1331 and 1255 cm<sup>-1</sup> are assigned to C-H wagging and amide III vibrations from proteins, respectively. The frequencies of amide I and III are consistent with those observed for disordered proteins.

**[0038]** Another example of a typical NIR FT Raman spectrum from normal aorta is shown in Figure 3. When irradiated from the intimal side, Figure 3a, the major vibrational bands observed in normal aorta are all attributable to protein vibrations: the band at 1658 cm<sup>-1</sup> is assigned to the amide I vibration of the polypeptide chain, the 1453 cm<sup>-1</sup> band to a C-H bending mode of proteins, and the 1252 cm<sup>-1</sup> band to the amide III vibration. The spectrum of normal aorta is at least 25% weaker than any of the pathologic samples. The peak frequency of the C-H bending band, which averaged for all the normal specimens is 1451±1 cm<sup>-1</sup>, is specific to the protein C-H bending mode (See below). The weak band near 1335 cm<sup>-1</sup>, which appears as a shoulder in many of the normal specimens, appears to be specific to elastin, and the weak band at 1004 cm<sup>-1</sup> is likely due to phenylalanine residues. In general, the relative intensities of the bands in the region between 1250 and 1340 cm<sup>-1</sup> appears very much like that observed in the FT Raman spectrum of elastin. This observation is consistent with the thin collagenous intima in normal aorta, the elastic nature of the media of aorta, and the deep penetration depth of 1064 nm radiation. Band assignments for all tissue types presented here are listed in Table 2.

**[0039]** Figure 3b displays the NIR FT Raman spectrum of the adventitial side of normal aorta. In this case, the irradiated adventitial surface consisted of several millimeters of visible adipose tissue. In contrast with the spectrum collected from the intimal side, the bands observed in this adipose material appear to be mainly due to lipid, and in particular triglyceride, with almost no contribution from protein. This is not unexpected, as the triglyceride content of adipose tissue is on the order of 60%. The sharp band at 1655 cm<sup>-1</sup> is due to stretching of C=C groups in unsaturated fatty acid chains. This band is distinguished from amide I by its peak frequency and its width, which in this case is 17 cm<sup>-1</sup> FWHM. Amide I, in contrast, is roughly 60 cm<sup>-1</sup> wide. The dominant C-H bending band is shifted to 1440 cm<sup>-1</sup>, characteristic of lipids. This band is about 3 times more intense in adipose tissue than in normal intima, probably a result of the greater number of C-H groups per unit volume in triglycerides. The bands at 1301/1267 cm<sup>-1</sup> and 1080 cm<sup>-1</sup> are assigned to C-H bending and C-C stretching vibrations of fatty acids, respectively.

**[0040]** The 1746 cm<sup>-1</sup> band, assigned to the C=O stretching mode of the triglyceride ester linkages, indicates that most of the lipid observed in the adventitial adipose tissue is of the triglyceride form. Specifically, the integrated intensity of this band relative to the C-H bending band at 1440 cm<sup>-1</sup> is equal to 0.103, while this same ratio for triolein is 0.136, which indicates that roughly 75% of the C-H band is due to triglyceride. The NIR FT Raman spectrum of triolein (a triglyceride containing fatty acid chains of 18 carbons and a single double bond) is shown for comparison in Figure 3c. Additional molecular information regarding the state of the fatty acid chains is readily deduced from the adventitial adipose spectrum. For example, the relative intensity of the C=C band at 1655 cm<sup>-1</sup> indicates that there are on average roughly 0.7 unsaturated double bonds per fatty acid chain, assuming 16-18 carbon fatty acids. In addition, the frequencies and structures of the C-H bending and C-C stretching bands suggest that most of the fatty acid chains are in the *gauche* conformation. The sharp 1129 cm<sup>-1</sup> band, characteristic of all-*trans* chains, is not observed in the spectrum.

**[0041]** The FT-Raman spectrum obtained from a diseased artery, an atheromatous plaque, with a thick fibrous con-

nective tissue cap and an underlying necrotic core is shown in Figure 2b. The necrotic core of an atheromatous plaque contains cellular debris as well as large accumulations of oxidized lipids and cholesterol. The band in the amide I region, peaking at  $1665\text{ cm}^{-1}$ , is distinctly narrower in this spectrum compared to normal aorta. In addition, the in-plane C-H bend, at  $1444\text{ cm}^{-1}$ , is relatively more intense and has a distinct shoulder at higher frequency. The two weaker bands at  $1307$  and  $1267\text{ cm}^{-1}$  are shifted in frequency from those found in the spectrum of normal aorta. The band frequencies and shapes in the FT-Raman spectrum of cholesterol, shown in Figure 2c, coincide with some of those observed in the atheromatous plaque, consistent with the expected composition of the necrotic core.

**[0042]** The NIR FT Raman spectra of other fibrous plaque specimens exhibit a range of features as shown in Figures 4 and 5. Figure 4a shows a representative spectrum from one of the types of fibrous plaques. These fibrous plaque spectra are quite similar in both relative and absolute band intensities to the spectra of normal aorta. The most significant differences are that the C-H bending band, peaking near  $1448\text{ cm}^{-1}$  on average, is shifted by  $2\text{ cm}^{-1}$  to a slightly lower frequency. This may be the result of a small increase in the lipid content of these plaques relative to normal aorta. In addition, the band near  $1340\text{ cm}^{-1}$ , attributed to elastin in normal aorta, is decreased relative to amide III at  $1265\text{ cm}^{-1}$ . The putative explanation is that the collagenous intima is thickened in these specimens, so that the spectral contribution from the elastic media is reduced relative to that of normal aorta.

**[0043]** The NIR FT Raman spectra of other fibrous plaque specimens appeared similar to atheromatous plaques' spectra (Figure 2b). These are substantially different than either normal aorta, or adipose tissue. In these cases, the intense C-H bending band occurs at  $1440\text{ cm}^{-1}$ , characteristic of lipid material. This band is roughly twice as intense as the C-H bending band in normal aorta. The complete absence of a band at  $1746\text{ cm}^{-1}$  indicates that this lipid is not triglyceride. In fact, this lipid appears to be predominantly cholesterol, as identified by the sharp, characteristic band at  $700\text{ cm}^{-1}$  and comparison to the cholesterol spectrum shown in Figure 4c. Again, this is not surprising, since cholesterol accumulates in high concentrations in atherosclerotic lesions. Several of the bands between  $1000$  and  $500\text{ cm}^{-1}$  are assignable to vibrational modes of the sterol rings. These include the bands at  $959$ ,  $882$ ,  $844$ ,  $805$ ,  $700$ ,  $605$ , and  $546\text{ cm}^{-1}$ . In addition, the  $1666\text{ cm}^{-1}$  band is attributed in part to the C=C stretching vibration of the steroid nucleus.

**[0044]** The presence of fatty acid chains in the atheromatous plaque spectra is evidenced by bands at  $1300/1262\text{ cm}^{-1}$  and  $1130/1088\text{ cm}^{-1}$ , due to C-H bending and C-C stretching vibrations, respectively. These bands may contain contributions from cholesterol as well. The relative intensities of the fatty acid band at  $1300\text{ cm}^{-1}$  and the sterol ring bands suggest a mixture of free cholesterol and cholesterol-fatty acid esters. Moreover, the relative intensities of the  $1130\text{ cm}^{-1}$  C-C stretching and the  $700\text{ cm}^{-1}$  sterol bands indicate that most of the fatty acid chains are in the *gauche* conformation, consistent with the predominance of unsaturated fatty acid chains in the cholesterol esters in these plaques. It is particularly noteworthy in the atheromatous plaques that the cholesterol deposits are detected from material below a thick fibrous cap indicating the ability of the NIR FT Raman method to probe materials several hundred microns below the tissue surface.

**[0045]** In addition to the cholesterol and cholesterol ester bands, the NIR FT Raman spectra of some of the fibrous plaques contained two unique bands, at  $1519$  and  $1157\text{ cm}^{-1}$ . The intensities of these bands are highly correlated, which suggests that they are due to a single component. These bands, which have been previously observed in visibly-excited Raman spectra of atherosclerotic plaques, are assigned to carotenoids. The amount of carotenoid in these plaques is probably much smaller than the amounts of cholesterol or proteins, but may be strongly pre-resonance enhanced (14). The carotenoid bands are observed only in this subset of fibrous plaques.

**[0046]** In an advanced plaque, calcium may begin to accumulate leading to the formation of calcium hydroxyapatite crystals in the tissue as shown by the spectra of Figures 5 and 6. The FT-Raman spectrum of a calcified plaque with a thick (several hundred microns) fibrous connective tissue cap overlying a calcified deposit is shown in Figure 5a. The spectrum clearly indicates bands due to the protein in the fibrous cap, amide I and III at  $1665$  and  $1255\text{ cm}^{-1}$ , respectively. However, additional bands are observed between  $1250$  and  $1350\text{ cm}^{-1}$  and around  $1100\text{ cm}^{-1}$ , as well as a strikingly sharp band at  $961\text{ cm}^{-1}$ . The latter is readily assigned to the symmetric phosphate stretching vibration associated with phosphate groups in the calcium hydroxyapatite deposits, while the band around  $1100\text{ cm}^{-1}$  is an asymmetric phosphate stretch. These assignments are confirmed by excising the solid "rock" from a different calcified plaque, and obtaining its spectrum as shown in Figure 5b. A strong Raman signal from the phosphate stretching vibration in solid calcifications in advanced atherosclerotic plaques can also be observed utilizing standard visible Raman instrumentation. The ability to detect the calcifications several hundred microns below the tissue surface when using near IR FT-Raman spectroscopy, however, is a diagnostic measurement which can be utilized to guide treatment.

**[0047]** A measurement was attempted to determine if the calcification might be detected when the tissue was irradiated from the adventitial side. The resulting FT-Raman spectrum is shown in Figure 5c. No evidence of the strong phosphate vibration is apparent. In contrast, sharp vibrational bands at  $1745$ ,  $1656$ ,  $1444$ ,  $1303$ ,  $1267$  and  $1082\text{ cm}^{-1}$  are observed which are mainly associated with the lipid material that constitutes the majority of the adventitia.

**[0048]** The NIR FT Raman spectrum of calcified plaque, containing a subsurface calcified deposit and an overlying soft fibrous cap, exhibits an intense, sharp, new band at  $960\text{ cm}^{-1}$  (Figure 6a). This band, specific to calcified tissue, is assigned to the symmetric stretching vibration of phosphate groups (15), which are present in high concentrations in

the solid calcium salts. The weaker phosphate antisymmetric stretch is also present at  $1072\text{ cm}^{-1}$ . A symmetric stretching vibration of carbonate groups may also contribute to this latter band. The phosphate vibrations are easily observed from subsurface deposits in the calcified plaques: the  $960\text{ cm}^{-1}$  band can be observed from deposits up to 1.5 mm beneath a soft tissue cap with the current signal-to-noise level (See below). The calcified plaque also displays protein vibrations from the fibrous tissue cap. These include amide I at  $1664\text{ cm}^{-1}$  and amide III near  $1257\text{ cm}^{-1}$ . The C-H bending band at  $1447\text{ cm}^{-1}$  suggests a mixture of protein and lipid, and the weak band at  $699\text{ cm}^{-1}$  is likely due to cholesterol that is either in the fibrous cap, the calcified deposit, or both.

**[0049]** The NIR FT Raman spectra of exposed calcifications (Figure 6b) display a range of features. In all cases, the major bands are due to the calcium salts. These include the  $960\text{ cm}^{-1}$  phosphate and  $1072\text{ cm}^{-1}$  phosphate/carbonate bands as well as the band at  $587\text{ cm}^{-1}$ , which is assigned to another phosphate vibrational mode. On the other hand, several differences are apparent in the weaker bands, which are presumably due to soft tissue components which are embedded in the calcification. In some cases (not shown), the C-H bending band occurs at  $1450\text{ cm}^{-1}$ , and the band at  $1663\text{ cm}^{-1}$  is similar in shape to amide I for some of the calcifications, indicative of protein vibrational modes. In other calcified plaques, such as that in Figure 5b, the C-H bending band occurs at  $1440\text{ cm}^{-1}$ , and the  $1667\text{ cm}^{-1}$  band, which is much sharper, is more like due to C=C stretching vibrations. In this plaque, the bands are due to lipid, in particular cholesterols, as evidenced by the  $700\text{ cm}^{-1}$  and  $1300\text{ cm}^{-1}$  bands.

**[0050]** In our histological examinations of aorta, two distinct types of exposed calcifications have been noted. In one type, the fibrous tissue cap is calcified. In the other, the necrotic core of an atheromatous plaque is calcified, and the calcified deposit is exposed by ulceration of the soft tissue fibrous cap. A positive explanation for the two spectral types of exposed calcifications is that the specimens which exhibit protein bands are of the former histologic type, while the specimens which exhibit lipid bands are of the latter type.

**[0051]** The present methods provide an IR FT-Raman technique for differentiating various stages of atherosclerosis in human aorta. They demonstrate that molecular level information is available using these methods. This information is useful for following the pathogenesis of the disease and in guiding the treatment of different lesions. The near IR FT-Raman method, with its relatively deep penetration depth, is able to obtain spectroscopic signals from below the tissue surface, yielding details about the atheromatous necrotic tissue and sub-surface calcifications. These signals can be utilized with an optical fiber based imaging system to determine the content and composition of different atherosclerotic plaques in vivo.

**[0052]** With the observation that several of the biochemical species important in the atherosclerotic process, including cholesterol and calcium hydroxyapatite, can be easily detected below the tissue surface, we wished to determine the depth limit of detection using the NIR FT Raman technique. In order to address this question, ten  $200\text{ }\mu\text{m}$  sections of aortic media were cut and placed one at a time over a large calcified deposit ( $6\times 6\times 3\text{ mm}$ ), and the FT Raman spectra of the  $960\text{ cm}^{-1}$  band monitored as a function of depth below the surface. As indicated by the plot of FT Raman intensity versus depth shown in Figure 7, the signal from the calcified deposit was detectable until the deposit was greater than 1.6 mm below the irradiated surface. Even slightly deeper depths could be probed if the focus of the collection optics was moved into the tissue.

**[0053]** The two dimensional resolution of the NIR FT Raman signal for material below the tissue surface was then tested by placing 1 nun of aortic media above another calcified deposit, and moving the tissue transversely in two dimensions through the laser beam and collection lens. The FT Raman signal was observed to drop-off rapidly as the beam and collection optics moved from the calcified deposit. The detected FT Raman signal closely followed the geometry of the calcified deposit below the surface, despite the significant scattering of the overlying layer of tissue. This result suggest that the Raman scattered light may be utilized for imaging objects below the tissue surface with minimal image blurring due to elastic scattering in the tissue.

**[0054]** A second spectroscopic method is also used to obtain molecular vibration information, attenuated total reflective (ATR) of infrared light.

**[0055]** Human aorta was chosen as an example to illustrate the diagnosis of atherosclerotic artery tissue. As in the samples obtained for the Raman spectral measurements human aorta samples were obtained for ATR measurements at the time of post mortem examination. Sample storage and preparation procedures are identical to those set forth for the Raman spectral measurements. These reflectance measurements can be used by themselves to provide diagnostic data in conjunction with either the Raman spectroscopic measurements described above or with fluorescence measurements, or with both types of measurements to enhance diagnosis for specific applications.

**[0056]** The medial layers of a normal arteries and the necrotic cores of atheromatous plaques were exposed by blunt dissection and spectroscopically examined. ATR spectra were also collected from several purified tissue components including collagen, elastin, and cholesterol to assist in analysis of the spectra.

**[0057]** Mid-infrared ATR spectra were measured from  $4000$  to  $700\text{ cm}^{-1}$  with a commercially available FT-IR spectrometer and a horizontal ATR accessory. The sampling area was purged with dry nitrogen gas to control background absorption from atmospheric water vapor and  $\text{CO}_2$ . Spectra were collected at  $4\text{ cm}^{-1}$  resolution with 50 scans. The artery specimens, kept physiologically moist with isotonic saline (buffered at pH 7.4), were placed in contact with the



ATR element (ZnSe crystal 45 ends). A 5 gram weight placed on the tissue sample ensured uniform sample contact with the ATR element. An ATR spectrum of the saline solution with absorbance similar to that of the artery samples was also obtained and used for subtraction of spectral components due to water. Collagen (Calbiochem: type I, bovine achilles tendon) and elastin (Sigma: bovine neck ligament) were prepared as saline slurries. Cholesterol (Sigma) was prepared as a dry film on the ATR element by evaporation of a benzene solution. These elements can be clearly identified in the resulting spectra.

**[0058]** The ATR sampling crystal is a rod of high refractive index material which acts as a waveguide for the infrared sampling beam. This waveguide can be in the form of a needle that is adapted for penetration into the tissue to be diagnosed. Alternatively, the probe will have a geometry suitable for contacting the surface of exposed tissue sites or for contacting internal locations with a catheter.

**[0059]** The devices shown in Figures 16A and 16B illustrate probes adapted for ATR diagnostic measurements within the human body. In Figure 16A a single-ended probe 100 is shown where one or more optical fibers 102 both the incident light to, and the transmitted (reflected) light from, the ATR element 104. A 100% infrared reflector 106 such as gold is placed at the distal surface 108 of the ATR element 104 functions to return the transmitted light back through the same fiber as well as to provide double pass sampling. The ATR element 104 can be a separate component optically fastened to the optical fibers 102, or alternatively, it can be constructed from the end of the optical fiber by removing the cladding material. Sampling is provided by placing the ATR element in contact with the tissue 110 of interest. Radiation is transmitted 112 and collected 114 in a radial direction from element 104. The probe can either be inserted through a standard endoscope or catheter to sample a hollow organ, or, if made with sufficiently thin optical fiber, it can be directly inserted directly into a solid organ as in the case of needle biopsy. In this particular embodiment the distal tip 108 is in the form of a needle. The cone or needle configuration on the end of the catheter can be long or shallow.

**[0060]** A double-ended probe is illustrated in Figure 16B. Incident IR beam from FT-IR is transmitted through IR optical fiber 122 to ATR element 128 positioned at the distal end of catheter body 120. The ATR element is placed in contact with tissue 126 surface to be sampled. Transmitted light is conducted through a second IR optical fiber 124 back to an IR detector. The ATR element may be a separate component optically fastened to the two optical fibers 122, 124, or it may be simply a region of a single optical fiber in which the fiber cladding material has been removed. The entire apparatus can be inserted through a standard endoscope or outer catheter.

**[0061]** For methods of measuring excised samples, the specimen to be sampled is placed in optical contact with the surface of the waveguide or ATR element. The evanescent wave which extends outside of the waveguide surface is absorbed by the sample in proportion to its absorption coefficient. The penetration depth of the evanescent wave into the sample depends on the wavelength of the infrared radiation and the refractive indices of the waveguide and the sample; for a ZnSe-water interface, this depth is roughly  $1 \mu\text{m}$  from  $1800$  to  $700 \text{ cm}^{-1}$ . The  $1/e$  penetration depth of the evanescent wave into the sample is given by  $\lambda/2\pi(n_z^2 \sin^2 \Theta - n_w^2)^{1/2}$ , where  $\lambda$  is wavelength,  $\Theta$  is angle of incidence and  $n_z$  and  $n_w$  are the refractive indices of ZnSe and water respectively. Consequently, only tissue that is in good optical contact with the ATR element will be sampled. In addition, individual components in the sample can exhibit different affinities for the waveguide material (ZnSe in this case), which can influence the relative concentrations of the components at the waveguide surface. Despite relatively high concentrations in the bulk tissue, components with poor optical contact can be difficult to measure in the ATR spectrum.

**[0062]** Figure 8 shows FT-IR ATR spectra of (a) normal aorta (intimal side) and (b) buffered saline. A comparison of these spectra shows that a majority of the IR absorption of normal intima can be attributed to water, which comprises roughly 80% of the tissue by weight. The large, broad bands peaking at  $3300 \text{ cm}^{-1}$  and  $1636 \text{ cm}^{-1}$  are due to the O-H stretching and H-O-H bending vibrations, respectively, of water, and the weak band at  $2120 \text{ cm}^{-1}$  is due to a water combination vibration. The  $3300 \text{ cm}^{-1}$  and  $1636 \text{ cm}^{-1}$  bands also include contributions from the N-H stretching and amide I vibrations. The relatively flat absorption between  $1500$  and  $900 \text{ cm}^{-1}$  and the rising absorption below  $900 \text{ cm}^{-1}$  is also due primarily to water; however, in the intima, a number of very weak bands due to other tissue components are also present in this region.

**[0063]** Most biomolecules give rise to IR absorption bands between  $1800$  and  $700 \text{ cm}^{-1}$ , which is known as the "fingerprint region" or primary absorption region. The dominant absorption of tissue water in this region obscures the absorption bands from other tissue components. To observe the IR bands from these components, one must eliminate the water interference. With the ATR method, spectral deconvolution or subtraction of the water component is particularly easy. By using the  $2120 \text{ cm}^{-1}$  band, which is due solely to water, as an internal intensity standard the spectrum of buffered saline (Figure 8b) can be accurately and reliably subtracted from the spectrum of aorta intima (Figure 8a), yielding a water-subtracted spectrum of intima (Figure 9a).

**[0064]** In the water-subtracted spectrum, the previously weak bands are easily observed. Band assignments, based on the spectra of the major tissue components are listed in Table I. Most of the vibrational bands observed in the spectrum of normal intima (Figure 9a) can be divided into two broad categories: lipid-associated bands and protein-associated bands. All of the strong bands in normal intima are associated with one of these moieties (see Table I). This can be seen as a simple consequence of the large concentrations of these two materials. Aside from water, a large frac-

tion of tissue can be divided into one of these two groups. Moreover, both protein and lipid components contain repeating molecular units which are common to all members of the group. For

Table I

Preliminary assignments of IR absorption peaks in the ATR spectra of normal aorta intima.		
V ( $+1\text{cm}^{-1}$ )	Preliminary Vibrational Assignment	Associated Tissue Components
2923(s)	C-H stretch	Lipid, Protein, Others
2853(s)	C-H stretch	Lipid, Protein, Others
1744(s)	C=O (ester) stretch	Lipid
1651(s)	Amide I	Protein
1635(sh)	Amide I, H-O-H bend	Protein, Water
1548(s)	Amide II	Protein
1465(s)	CH <sub>2</sub> bend	Lipid
1457(s)	CH <sub>2</sub> bend, CH <sub>3</sub> anti-symmetric deformation	Lipid
1454(s)	CH bend, CH <sub>3</sub> anti-symmetric deformation	Protein, others
1417(w)	CH <sub>2</sub> bend adjacent to C=O	Lipid
1401(m)	COO <sup>-</sup> symmetric stretch, amide C-N stretch	Protein, others
1378(w)	CH <sub>3</sub> symmetric deformation	Lipid
1244(m)	Amide III, PO <sub>2</sub> <sup>-</sup> anti-symmetric stretch	Protein, others
1239(m)	CH <sub>2</sub> wag, PO <sub>2</sub> <sup>-</sup> anti-symmetric stretch	Lipid
1159(s)	CH <sub>2</sub> wag, C-O-C antisymmetric stretch	Lipid
1117(w)	C-C stretch, O-C-O stretch	Lipid
1096(w)		Lipid
1083(w)	PO <sub>2</sub> <sup>-</sup> symmetric stretch	Protein, others
1030(w)		Lipid
965(w)	C=CH deformation (trans)	Lipid
722(m)	CH <sub>2</sub> rock	Lipid

Table II

Peak frequencies of selected bands in normal and atherosclerotic aorta.						
Normal	Adventitia <sup>a</sup>	Fibrous Plaque	Fatty Plaque	Exposed Cal-cif.I	Exposed Cal-cif.II	Assignments
	1746w					C=O (ester) stretch
	1667m	1667m		1667m		C=C Stretch Lipid
1658s				1663m		Amide I (8)
	1655m					C=C stretch Fatty Acids
		1519w				Carotenoid (12)
1451s				1450s		C-H bend (8)
	1440s	1440s	1440s		1440s	Protein Lipid
	1301m	1301w	1301w		1300w	Lipid C-H bend
	1267w	1264w	1262w		1262w	(CH <sub>2</sub> ) Lipid C-H bend (=C-H)
1252m				1261w		Amide III (8)
		1157w				Carotenoid (12)
	1080m	1131w 1086w	1130w 1088w	1128w		C-C stretch Lipid
				1071s	1071s	Phosphate antisymmetric stretch Calcium salts (15)
1004w		1004w	1004w			Phenylalanine (8)
				960vs	960vs	Phosphate symmetri stretch Calcium salts (15)

Table II (continued)

Peak frequencies of selected bands in normal and atherosclerotic aorta.						
Normal	Adventitia <sup>a</sup>	Fibrous Plaque	Fatty Plaque	Exposed Cal-cif.I	Exposed Cal-cif.II	Assignments
		957w 882w 842w 803w 700m 606w 546w	956w 882w 841w 801w 700m 606w 546w		878w 850w 804w 699m 547w	Cholestreols (11)
				587m	587m	Phosphate Calcium salts (15)
Peak frequencies of typical specimens, accurate to $\pm 1$ cm <sup>-1</sup> . Abbreviations: vs=very strong, s=strong, m=medium, and w=weak relative band intensity.						

<sup>a</sup>Adventitia specimen is mainly adipose tissue.

protein, the polypeptide backbone of repeating amide groups is the dominant element. In lipids, the repeating hydrocarbon chain is the defining quality. The end result is that these molecular units are present in very large concentrations, and their vibrational bands tend to dominate the spectrum. Note that this does not imply that no further level of detail is derivable from the IR spectrum of tissue. For example, the frequencies of the amide group vibrations are sensitive to protein configuration and conformation. Therefore, shifts in protein makeup might be expected to produce observable changes in the amide bands.

**[0065]** The water-subtracted spectrum of sub-adventitial fat shown in Figure 9b, more clearly illustrates the division of bands into lipid and non-lipid categories. This fat can be considered as the model of the lipid component. Protein contributions, as judged from the intensities of the amide I and II bands, are negligible for the purposes of this model. All of the bands observed in the fat spectrum can be attributed to the lipid component. These include the strong bands at 1744 cm<sup>-1</sup> (C=O stretch), 1465 cm<sup>-1</sup> (C-H bend), 1161 cm<sup>-1</sup> (CH<sub>2</sub> wag, C-O-C stretch), as well as the weaker bands at 1378 cm<sup>-1</sup>, 1239 cm<sup>-1</sup>, 1118 cm<sup>-1</sup>, 1099 cm<sup>-1</sup>, 966 cm<sup>-1</sup>, and 722 cm<sup>-1</sup>.

**[0066]** The bands observed in the water-subtracted spectrum of intima constitute less than 30% of the total absorption, the rest being due to water. Any conclusions regarding these relatively weak bands depends critically upon the accuracy of the water subtraction. The accuracy of this subtraction can be judged from the reproducibility of spectra obtained sequentially from the same sample. Two consecutive water-subtracted spectra collected 10 minutes apart from a sample of normal aorta (intimal side) are shown in Figure 10a (solid and dashed curves). Most of the IR bands exhibit a substantial increase in absorbance with time. This trend continues for consecutive spectra collected more than an hour after the placement of the sample on the APR element. However, not all of the bands change by the same fraction, so that the relative intensities differ between consecutive spectra. For instance, in Figure 10a, the C=O band at 1744 cm<sup>-1</sup> is relatively constant, while the amide bands at 1650 cm<sup>-1</sup> and 1547 cm<sup>-1</sup> increase by 50% in the later spectrum. Although these changes might seem to indicate that the water subtraction is inaccurate, the changes with time are systematic and predictable, which suggests that the optical contact between the sample and the ATR element is changing regularly with time.

**[0067]** In fact, the constancy of the 1744 cm<sup>-1</sup> C=O band, which is due solely to lipid, and the increases in the amide bands, which are due to protein, indicate that the lipid contributions to the IR absorption remain unchanged while the non-lipid contributions increase between consecutive scans. This is confirmed by subtracting the spectrum of lipid (Figure 9b) from the water-subtracted spectra of aorta intima (Figure 10a), using the 1744 cm<sup>-1</sup> band for normalization. The resulting lipid-subtracted spectra of aorta intima are shown, normalized to peak absorbance, in Figure 10b. As can be seen, the relative peak absorbencies and spectral bandshapes in the lipid-subtracted spectra reproduce quite well, reflecting the accuracy of both the water and the lipid-subtraction procedures.

**[0068]** The constancy of the lipid bands and the variation of the non-lipid bands between successive scans may seem somewhat puzzling. An explanation of this apparent anomaly can be inferred from a water-subtracted spectrum of saline solution which is rinsed off the surface of the tissue (Figure 9c). This spectrum, aside from the weak amide I and II bands, matches quite closely with that of adventitial fat. The lipid component observed in the tissue appears to be due to free lipid particles that have equilibrated with the tissue surface water, forming a thin water-lipid film on the tissue surface which is in full optical contact with the ATR element immediately after the tissue specimen is placed upon the crystal. The tissue components beneath this film presumably achieve better optical contact with the ATR crystal as the sample settles. As a result, the content of lipid in a spectrum of aorta intima or media may be influenced by the presence of sub-adventitial fat in the specimen, and the relative lipid-protein absorbencies are accurate to 50% at best with the present experimental design. For the reason, all of the remaining spectra shown are both water and lipid subtracted.

**[0069]** With the lipid bands removed, assessment of the non-lipid bands in the spectrum of normal intima (Figure 10b) is greatly simplified. The major bands in the spectrum may be assigned to protein backbone vibrations. These include the bands at  $1648\text{ cm}^{-1}$  (amide I),  $1549\text{ cm}^{-1}$  (amide II),  $1455\text{ cm}^{-1}$  (C-H bend),  $1401\text{ cm}^{-1}$  (amide C-N stretch), and  $1244\text{ cm}^{-1}$  (amide III). The frequency of the amide I peak ( $1648\text{ cm}^{-1}$ ), which is sensitive to protein secondary structure, may indicate contributions from  $\alpha$ -helix, disordered, and collagen helix conformations. This band also exhibits a shoulder near  $1634\text{ cm}^{-1}$ , which may be due to the  $\beta$ -sheet regions of proteins or water. The protein C-H bending band at  $1455\text{ cm}^{-1}$  is distinct from the corresponding vibration in lipid, which occurs as a double-peaked band at  $1465/1457\text{ cm}^{-1}$ . Note that all of these bands may include contributions from other moieties. For instance, the symmetric stretch of carboxylate groups and the antisymmetric stretch of phosphate groups may also contribute, respectively, to the  $1401\text{ cm}^{-1}$  and  $1244\text{ cm}^{-1}$  bands. This correlation of components is summarized in Table I above.

**[0070]** A typical spectrum of the medial layer of normal aorta is shown in Figure 11a. A comparison of this spectrum to that of normal intima (Figure 10b) fails to reveal any significant differences. This result is somewhat surprising, considering that normal aorta intima and media have significantly different compositions. Typical spectra of an atherosclerotic plaque and a non-ulcerated atheromatous plaque are shown in Figures 11b and 11c, respectively. For these plaques, only the intact fibrous cap at the intimal surface is probed due to the short penetration depth ( $1\text{ }\mu\text{m}$ ) of the beam. Any necrotic, atheromatous material beneath this fibrous cap is not sampled. Even so, the fibrous caps of these plaques are known to be compositionally different than normal intima and one might expect these differences to be reflected in the IR ATR spectrum. However, as in the case of media, no consistent differences are observed in the spectra of these plaques (Figures 11b and 11c) and normal intima (Figure 10b). This issue will be expanded upon in the discussion below.

**[0071]** On the other hand, substantial differences are obvious in the spectrum of the necrotic, atheromatous core of an atheromatous plaque (Figure 12a) as compared with the corresponding spectra of normal intima (Figure 10b) as well as those of intact atherosclerotic (Figure 11b) and atheromatous (Figure 11c) plaques. In this case, the necrotic core was presumably exposed in vivo as disease progressed by ulceration of the overlying intimal fibrous tissue cap. (The spectrum of necrotic core exposed by dissecting away the fibrous cap of a non-ulcerated atheromatous plaque is similar.) A new band appears at  $1050\text{ cm}^{-1}$ , with a secondary peak at  $1023\text{ cm}^{-1}$ . In addition, the necrotic core spectrum exhibits an increase and frequency shift in the  $1466\text{ cm}^{-1}$  band as compared with the  $1455\text{ cm}^{-1}$  protein band in normal intima as well as a set of unique bands near  $1382\text{ cm}^{-1}$ . These characteristic bands are found in the spectra of all the exposed necrotic core samples and in none of the other samples (see below).

**[0072]** The source of these unique bands in the necrotic core spectra may be cholesterol, which is known to accumulate in large amounts in atheromatous cores. An ATR spectrum of cholesterol (dry film) is shown in Figure 12b. The three major bands unique to the necrotic core, near  $1463\text{ cm}^{-1}$ ,  $1382\text{ cm}^{-1}$ , and  $1050\text{ cm}^{-1}$ , match closely in position and relative intensities with the three main cholesterol bands at  $1466\text{ cm}^{-1}$ ,  $1377\text{ cm}^{-1}$ , and  $1056\text{ cm}^{-1}$ . Each of the main cholesterol bands has a secondary peak, which also appears to be present in the necrotic core bands. These secondary peaks occur at  $1445/1436\text{ cm}^{-1}$ , and  $1023\text{ cm}^{-1}$  in the cholesterol spectrum and at  $1441\text{ cm}^{-1}$ ,  $1367\text{ cm}^{-1}$ , and  $1023\text{ cm}^{-1}$  in the necrotic core spectrum. In addition, several of the weak bands in the necrotic core spectrum, including the peaks at  $1334\text{ cm}^{-1}$ ,  $1109\text{ cm}^{-1}$ ,  $954\text{ cm}^{-1}$ , and  $797\text{ cm}^{-1}$ , are associated with the weaker cholesterol bands near these frequencies. Other components in the necrotic core may also contribute to some of these distinct bands.

**[0073]** The consistency of the spectral differences which are attributed to cholesterol between the necrotic core specimens and the normal, atherosclerotic, and non-ulcerated atheromatous specimens are illustrated in the scatter plot in Figure 13. This plot depicts the integrated intensities (areas) of the  $1050\text{ cm}^{-1}$  cholesterol band ratioed to the total protein content, as measured by the area of the amide II band at  $1548\text{ cm}^{-1}$ . The  $1050\text{ cm}^{-1}$  band was integrated from  $1075$  to  $1000\text{ cm}^{-1}$  and baseline subtracted using these endpoints, and the amide II band was integrated from  $1593$  to  $1485\text{ cm}^{-1}$  with a similar baseline subtraction. This ratio is a measure of the relative cholesterol contribution to the spectrum, and is proportional to the relative cholesterol concentration of the sample with the assumption that the area of the  $1050\text{ cm}^{-1}$  band is due solely to cholesterol. As can be seen in Figure 13, this ratio is higher for all the exposed necrotic core specimens than for all the other specimens. The consistent results of this sample analysis, which is possible because of the separation and molecular identification of the bands, indicates the potential of IR spectroscopy for tissue

characterization.

**[0074]** Investigations of human arteries and atherosclerosis by mid-IR spectroscopy have been limited to date. It has been reported that ATR spectra have been recorded from partially dried human artery, among other tissues. In comparing a normal aorta from an infant to an atherosclerotic plaque in an adult, they observed increases in several bands in the atherosclerotic aorta. Most of these bands were associated with lipids and lipoproteins. IR spectroscopy has been employed to determine the chemical composition of calcified atherosclerotic deposits. A more detailed IR study of atherosclerotic aorta involves recorded IR transmission spectra from thin layers sectioned at different depths into the arterial wall. Results showed increased absorption near  $1739\text{ cm}^{-1}$  in the fatty (atheromatous) regions of plaque, which was attributed to absorption by cholesterol esters in the plaque. IR spectra from the fibrous tissue cap at the surface of the plaques were similar to normal intima.

**[0075]** One of the main difficulties in measuring mid-infrared spectra of intact human tissue is the intense water absorption, which dominates and obscures the absorption of other tissue components of interest. In most of the studies cited above, the water absorption was not eliminated, limiting the quality and amount of information available from the spectra. With the ATR sampling method, this water interference is easily removed (see Figure 9). The ATR method is also naturally amenable to sampling with fiber optic probes *in vivo*. Water interference in fiber optic probe ATR spectra of aqueous protein solutions has been accurately eliminated with a water subtraction procedure similar to the one employed in the present study.

**[0076]** While the ATR method is well suited to *in vivo* sampling and to accurate subtraction of the water signal, spectra collected with the ATR method are not equivalent to ER absorption spectra, but depend on properties of the ATR material and the sample in addition to the sample absorption coefficient. For instance, the penetration depth of the evanescent sampling wave depends on the refractive indices of the ATR material and the sample. However, the refractive indices of both ZnSe and human tissue are expected to vary slowly with frequency between  $1800$  and  $700\text{ cm}^{-1}$  and such variations will at most affect the relative intensities of bands at different frequencies. All of the structure observed in the tissue spectra is attributed to absorption bands in the tissue.

**[0077]** The component absorptions observed in an ATR spectrum also depends upon the optical contact of the sample and ATR element. The small penetration depth of the evanescent wave into the tissue sample implies that only a  $5\text{ }\mu\text{m}$  thick layer, and preferably about 1 micron, of material at the surface is observed. This is referred to as the near surface region of the tissue for the purposes of this application. The tissue deeper than 5 microns from the surface is defined as the sub-surface region. This thin, sampled near-surface layer may differ in composition with the bulk sample. For example, a film of free water may be present on the surface of wet tissue, with different levels of some molecular species of the tissue relative to their concentrations in the bulk tissue. In addition, the varied affinities for the ATR material of different moieties in the tissue may play an important role in the intensities of the observed bands.

**[0078]** These considerations may explain the lack of substantial differences among the ATR spectra of normal intima, plaque fibrous cap, and media. For instance, normal aorta intima is composed of roughly 25% collagen (dry weight) and 20% elastin, while aorta media has 20% collagen and 50% elastin. The ATR spectra of purified collagen and purified elastin (not shown) differ substantially. In particular, amide I/II occur at  $1657/1556\text{ cm}^{-1}$  in hydrated collagen (type I) and  $1653/1543\text{ cm}^{-1}$  in hydrated elastin (spectra not shown).

**[0079]** One might expect these differences to be reflected in the intima and media ATR spectra. A possible explanation of why this is not the case is that the thin layer in optical contact with the ATR element is compositionally different from the bulk tissue, and collagen and elastin make only a minor contribution to the IR ATR bands of this layer. Such an effect may also explain the lack of significant differences among the plaque fibrous cap intima and normal intima ATR spectra. In ATR elements made of other substances with different biochemical affinities, the spectral differences among these tissues can be substantially enhanced depending on the tissue type.

**[0080]** The results of the present investigation demonstrate that high quality water-subtracted spectra can be readily obtained from human tissue with the ATR technique. Similar results have been obtained in other mammalian tissues. Accurate removal of the water interference is crucial to isolating the relatively weak tissue absorption bands of lipid, protein, as well as other tissue components. It is worth noting that the observation of these relatively weak bands via spectral subtraction depends entirely upon quality of the tissue and saline spectra. For instance, the absorbance of the normal intima specimen (Figure 8a) between  $1500$  and  $900\text{ cm}^{-1}$  is approximately 0.06. In the water-subtracted spectrum (Figure 9a), the peak absorbencies range from 0.018 (30%) for the strongest bands to 0.003 (5%) for the weakest ones. The detection of a 0.003 absorbance peak in a subtracted spectrum with a 0.06 absorbance background requires a signal-to-noise ratio of 700 or better in the 100% baseline. Such a signal-to-noise is easily achieved with an FT-spectrometer. The high linearity, baseline stability, and wavelength precision of the FT-spectrometer are also obviously critical for accurate background subtraction.

**[0081]** While water subtraction is relatively easy and accurate with ATR, it may be substantially more difficult with other clinically applicable sampling techniques such as diffuse reflectance or photoacoustic sampling. These alternative sampling techniques are clinically useful, however, because of their longer tissue penetration depths (approximately  $10\text{ }\mu\text{m}$ ). As an alternative to water subtraction, one can exploit the properties of the spectral lineshape of water to elim-

inate the water signal by other computational methods. Specifically, the spectral lineshape of water varies rather slowly with frequency over much of the region of interest, especially between 1500 and 700  $\text{cm}^{-1}$ . Therefore, any method which filters this slower variation and spares the sharper features of the non-water bands can separate the water and non-water components.

**[0082]** One such method is second derivative spectroscopy. Differentiation of a spectrum is typically used to narrow absorption bands and resolve overlapping peaks. Differentiation also tends to deemphasize broad bands relative to sharper ones. In IR spectra of artery, the broad, featureless absorption of water can be nearly eliminated in favor of the sharper non-water bands by computing the second derivative of the spectra. This is clearly demonstrated in Figure 14, which shows the second derivative of a spectrum of normal aorta intima (Figure 14a), along with the water-subtracted spectrum of the same specimen (Figure 14b). Essentially only the 1633  $\text{cm}^{-1}$  water band is left, partially obscuring the amide I band. Elsewhere in this spectrum, the water contribution is minimal. All of the bands identified in the water-subtracted spectrum are easily observed in the second derivative spectrum.

**[0083]** In addition to elimination of water interference, several of the unresolved double peaks and shoulders in the water-subtracted spectrum appear as distinct peaks in the second derivative spectrum. For example, the amide II band in normal intima (Figure 14b) has a very weak shoulder near 1518  $\text{cm}^{-1}$ , and the C-H bending region near 1468  $\text{cm}^{-1}$  appears to include two overlapping peaks. In the second derivative spectrum (Figure 14a), the 1518  $\text{cm}^{-1}$  band is clearly visible, and the C-H region exhibits two separate peaks at 1469 and 1456  $\text{cm}^{-1}$ . Moreover, by sharpening the bands, the second derivative spectrum allows a more precise determination of peak frequencies, so that relatively small frequency shifts are observed. Such frequency shifts can be of importance in detecting and characterizing subtle molecular alterations involved in certain tissue conditions.

**[0084]** The observation of individual, resolved bands in the artery IR ATR spectra is of considerable interest, since separation of bands is the first step determining the composition of a sample from its spectrum. Once a band has been isolated, its integrated intensity is proportional to the concentration of the moiety responsible for that band. In particular, since the amide I and II bands are due entirely to protein, these bands can be used to isolate the overall protein content in the spectrum. The sharp, well resolved 1744  $\text{cm}^{-1}$  C=O ester band appears to be due to solely to lipid, and the integrated intensity of this band should be proportional to the relative lipid content are technique should largely eliminate the inaccuracies. Finally, it should be remembered that the relative water content of the tissue sample is automatically computed from the 2120  $\text{cm}^{-1}$  band in the water subtraction algorithm. However, as noted earlier, the composition of tissue as determined from an ATR spectrum may not be precisely identical to the composition of the bulk tissue.

**[0085]** The tissue composition can also be determined from overlapping bands by first deconvolving the bands of interest into their individual components. This is especially easy if one component has an additional, isolated band elsewhere in the spectrum. An example is the 1465  $\text{cm}^{-1}$  C-H bending region, which is due to different tissue components with distinct spectral features in this region. In the normal intima spectrum (Figure 9a), this band is attributed to a combination of lipid and protein components. Since the lipid component also exhibits the isolated 1744  $\text{cm}^{-1}$  band, this band can be used to subtract the lipid C-H bending component and isolate the protein C-H bending component at 1455  $\text{cm}^{-1}$  (Figure 10b), effectively deconvolving this band. Note that this deconvolution depends on having a reliable spectrum of one of the individual components, which, in this example, is the lipid spectrum in Figure 9b.

**[0086]** The detection of distinct bands attributed to cholesterol in necrotic core may provide a useful means of determining cholesterol concentrations in vivo. Both the 1050  $\text{cm}^{-1}$  and 1382  $\text{cm}^{-1}$  cholesterol bands appear to be fairly isolated in the necrotic core spectrum after lipid-subtraction (Figure 12). If these two bands are due to a single component, namely cholesterol, the ratio of their integrated intensities should be a constant for all the samples. The baseline-subtracted area of the 1050  $\text{cm}^{-1}$  band,  $A(1050)$ , is plotted versus that of the 1382  $\text{cm}^{-1}$  band,  $A(1382)$ , for all the samples, normalized to the protein content in Figure 15. As can be seen in the plot, there is a roughly linear relationship between  $A(1050)$  and  $A(1382)$ . A linear least squares fit to this data yields the line shown in the plot, with a high regression coefficient of  $r=0.967$ . The slope of this line 2.8, while the ratio  $A(1050)/A(1382)$  for the pure cholesterol ATR spectrum is 2.3. The reasonable agreement between these two numbers provides additional evidence for the assignment of these bands to cholesterol. Moreover, it indicates that the relative spectral content of cholesterol is reasonably approximated by the integrated intensities of either of these bands. Figure 15 also shows that the ATR spectra of all the specimens other than exposed necrotic core exhibit almost no intensity in both the 1050 and 1382  $\text{cm}^{-1}$  bands, in contrast to the necrotic specimens, all of which have significant bands at both frequencies.

**[0087]** The present systems and methods demonstrate that infrared spectra of moist, bulk tissues can be reliably obtained with the ATR technique. Although water is the dominant absorber throughout much of the mid-infrared region, the high quality spectra acquired with the FT-IR ATR technique allow for accurate subtraction of the water signal. Elimination of the water interference is critical for identifying and assigning the absorption bands of other tissue species. The isolation and designation of these relatively sharp bands provides a means of analyzing spectroscopically the composition of arterial tissue non-destructively. These methods are also applicable to the study and diagnosis of other tissues and tissue conditions, such as neoplasia.

**[0088]** The observation of both lipids and cholesterol in the spectra of necrotic atheromatous core samples is par-

ticularly exciting, because lipids and cholesterol are thought to play major roles in the pathogenesis of atherosclerosis. The spectral observation of these components, cholesterol in particular, provides a reliable means of detecting and characterizing advanced atheromatous plaques in which ulceration of the fibrous cap has occurred (as demonstrated in Figures 13 and 15). Intimal accumulations of lipid and cholesterol occur early in the atherogenic process. Therefore, the mid-IR ATR technique can also be useful in detecting and studying the early fatty streak lesion.

## PRESENT INVENTION

### Spectrograph/CCD System for NIR Raman Spectra

**[0089]** NIR Raman spectroscopy using a single stage spectrograph and a charge coupled device (CCD) detector offers superior sensitivity over the Nd:YAG excited FT-Raman system of Figures 1A and 1C. By shifting the wavelength of the laser excitation from 1064 nm to the 800-900 nm region, a CCD can be used to detect the Raman scattered signals while still avoiding fluorescence excitation in most molecules. The system can operate usefully in the range of 750 nm to 1050 nm. Although the fluorescence emission from tissue is significantly higher with 810 nm than with 1064 nm excitation, the Raman signals are readily observed. This is because the dominant noise source in the spectrograph and CCD system is shot noise associated with the fluorescence emission, which is 2-3 orders of magnitude smaller than the dark current noise of the InGaAs detector, which is the dominant noise source in the FT-Raman system.

**[0090]** Figure 17 shows the laser diagnosis and treatment system of Figure 1A modified to use the spectrograph and CCD system of this invention. The diagnostic subsystem 201' includes a single stage spectrograph 310 and charge-coupled device (CCD) detector 312 for collecting near-infrared (NIR) Raman spectra from intact human arterial tissue. With 810 nm laser light excitation, preferably pulsed, the fluorescence emission from human artery tissue is sufficiently weak to observe Raman bands more rapidly with the spectrograph and CCD system than with the 1064 nm excited FT-Raman system of Figures 1A and 1C. A method for removing the broadband emission from the spectra by computing the difference of two emission spectra collected at slightly different excitation frequencies was used to enhance observation of the Raman bands. This method relies on the stability, linearity, and low noise characteristics of the CCD detector. The results indicate that high quality NIR Raman spectra can be collected in under 1 second with the spectrograph and CCD system and an optical fiber probe, as compared to 30 minutes with the FT-Raman system at similar laser power levels, further improving the use of the technique for *in vivo* clinical applications.

**[0091]** A preferred embodiment of a spectrograph and CCD system 300 employed for the collection of near infrared (NIR) Raman spectral data from excised tissue samples using a spectrograph and a charge coupled device (CCD) array is illustrated in Figure 18. NIR Raman spectra were measured from 100 - 2000  $\text{cm}^{-1}$  below the laser excitation frequency with a single stage imaging spectrograph 310 (Acton Model ARC275, 0.25 m, F/3.8) and a CCD array 312 (Princeton Instruments EEV Model 88130).

**[0092]** System 300 can use a NIR 810 nm Nd:YAG pumped pulsed dye laser 314 operating at 10 Hz for irradiating a sample 46. Alternatively, a CW or diode laser source can also be employed. Laser 314 generated a laser beam 316 which is directed by mirror 318 through focusing optics 320 to impinge on sample 46 mounted behind a transparent window 321. The laser beam was focused on the sample at a 70° angle of incidence, yielding a spot size of 0.7 x 2 mm on the tissue surface. The average incident power at the sample was maintained at 20 mW to avoid excessive peak intensities during an individual pulse. The spectral signals were observed to be linear over a range of average incident powers from 2 to 20 mW.

**[0093]** A portion of the scattered light 322 emitted by sample 46 was collected by collecting optics 324 at a 90° angle relative to the incident laser beam. Collecting optics 324 collimates and F/matches the collected light for the spectrograph 310. Prior to entering the entrance slit of the spectrograph 310, the collected light was passed through a series of Schott glass filters 326 which attenuated the elastically scattered component of the collected light. The combined effect of the Schott glass filters provided an optical density of 7 at 810 nm, a transmission of 20% at 850 nm (580  $\text{cm}^{-1}$  from 810 nm), and a transmission of 85% above 900 nm (1200  $\text{cm}^{-1}$ ).

**[0094]** The spectrograph 310 utilized a 200  $\mu\text{m}$  slit width and a 600 groove/mm grating blazed at 1  $\mu\text{m}$  and could be scanned to provide spectral coverage over different wavelength regions. The 200  $\mu\text{m}$  slit width provided a resolution of roughly 15  $\text{cm}^{-1}$ .

**[0095]** The CCD array 312 consisted of 298 (column) by 1152 (row) pixel elements having a total active area of 6.7 mm x 26 mm, with the short axis parallel to the slit. The CCD array was cooled to -110°C to eliminate dark current. Each row of pixels was binned to reduce readout noise. Commercially available CCD detectors offer extremely low detector noise and usable quantum efficiencies out to 1050 nm and provide substantial advantages over InGaAs and other NIR detectors. These advantages outweigh the lower throughput of the grating spectrograph, provided that broadband fluorescence interference is not too great with the shorter excitation wavelengths.

**[0096]** Excised human aorta samples 46 obtained at the time of post-mortem examination were rinsed with isotonic saline solution (buffered at pH 7.4), snap-frozen in liquid nitrogen, and stored at -85°C. Prior to spectroscopic examina-



tion, samples were passively warmed to room temperature and were kept moist with the saline solution. Normal and atherosclerotic areas of tissue were identified by gross inspection, separated, and sliced into roughly 8 x 8 mm pieces.

**[0097]** The tissue samples 46 were placed in a suprasil quartz cuvette with a small amount of isotonic saline to keep the specimens moist, and with one surface in contact with the transparent window 321 and irradiated by the laser 314.

**[0098]** Raman spectra were typically measured between  $100\text{ cm}^{-1}$  and  $2000\text{ cm}^{-1}$  below the laser excitation frequency. Each spectrum was background subtracted to remove the DC offset of the A/D converter of the CCD controller. In addition, hot pixels due to high energy radiation events were removed from the recorded spectrum by applying a median filter having a 7 pixel wide window as to each spectrum. Raman frequencies were calibrated with the spectra of benzene and barium sulfate powder and are accurate to  $\pm 5\text{ cm}^{-1}$ . The spectra were not corrected for the wavelength dependent response of the filters, spectrograph, and CCD. For each spectrum shown in the following Figures, Raman signals were accumulated for 5 minutes. Substantially shorter collection times can also be used as described herein.

**[0099]** Figure 19A shows the Raman spectra of a normal aorta sample excited with 810 nm laser light and collected with the spectrograph and CCD system 300. In this case, the broadband background emission, which is presumably due to tissue fluorescence, is roughly five times more intense than the strongest Raman bands at 1650, 1451, 1330, and  $1253\text{ cm}^{-1}$ . In contrast, the 1064 nm FT-Raman study of normal human aorta shown in Figure 2a exhibited Raman signals with the peak intensities of the strongest bands, amide I at  $1650\text{ cm}^{-1}$  and C-H bend at  $1451\text{ cm}^{-1}$ , being roughly three times larger than the broadband background emission. However, this background emission in the spectrograph and CCD system is relatively weak with respect to the Raman signals (i.e., on the order of the Raman signals) and therefore the shot noise associated with detecting this background emission is substantially smaller than the Raman signals, allowing the Raman bands to be made distinct after the background emission signals are removed through filtering or subtraction. The shot noise is typically random noise exhibiting a Poisson distribution and is associated with the detector and/or the background emission itself.

**[0100]** In contrast, with visible excitations, the fluorescence background emission from the arterial pathology tissue types described is 3 to 4 orders of magnitude larger than the Raman signals, and the shot noise associated with this stronger background emission completely obscures the Raman bands even after the background emissions are removed. However, certain other types of tissue, e.g., colon and bladder, do not exhibit such high level fluorescence reactions at visible excitation frequencies, and therefore can probably operate with visible excitations.

**[0101]** The signal-to-noise ratio of the spectrum of normal aorta collected with the spectrograph and CCD system 300 with 20 mW incident power and 5 minutes collection time (Figure 19A) is similar to that obtained with the FT-Raman system of Figure 1C with 500 mW incident power and 35 minute collection time. Since the observed spectral signal-to-noise ratios are similar, we estimate that the noise level observed with the CCD detector 312 of Figure 18 is roughly 3400 times less than that observed with the InGaAs detector 42 of Figure 1C. For the InGaAs detector, the major noise source is the shot noise of the dark current, while with the CCD detector the dominant noise source is the shot noise of the broadband tissue emission, as the dark current and readout electrons of the CCD are much smaller than this emission.

**[0102]** This simple analysis has several important implications. First, since the major noise source encountered with the spectrograph and CCD system is shot noise from broadband emission by the tissue sample, the spectral signal-to-noise ratio is proportional to the square root of the product of incident intensity and the collection time.

**[0103]** The FT-Raman and spectrograph and CCD systems can be compared as follows. For the FT-Raman system, the incident intensity is  $640\text{ mW/mm}^2$ . The quantum efficiency of the InGaAs detector at 1200 nm is 0.7, and the FT-spectrometer throughput is  $1.1\text{ mm}^2\text{sr}$ , and the transmission efficiency of the FT-spectrometer and filters is roughly 0.062. For the spectrograph and CCD system, the incident intensity is  $14\text{ mW/mm}^2$ . The CCD quantum efficiency is 0.15 at 900 nm, the spectrograph throughput is  $0.043\text{ mm}^2\text{sr}$ , and the transmission efficiency of the spectrograph and filters is 0.24. Combining these factors and taking into account the  $\nu^4$  dependence of the Raman cross-sections, the signal level measured by the FT-Raman spectrum is estimated to be 3400 times greater than that of the spectrograph and CCD spectrum.

**[0104]** Therefore, if the laser intensity is increased to the level employed in the FT-Raman experiments, the collection time could be reduced by a factor of 40, to 8 seconds, with no change in the spectral signal-to-noise ratio. Second, the noise level can be further reduced by using longer excitation wavelengths which minimize the tissue fluorescence emission. However, such reductions in fluorescence emission must be balanced against the decreasing quantum efficiency of the CCD at longer wavelengths, and the optimum excitation wavelength also depends on the fluorescence excitation profile of the tissue. For tissue types that exhibit little fluorescence emission at visible wavelengths, such as colon and bladder tissue, the CCD can be operated at visible or near visible wavelengths to take advantage of increased quantum efficiency of the CCD at these wavelengths. Finally, the throughput of a  $500\text{ }\mu\text{m}$  core, 0.2 numerical aperture fused silica optical fiber is  $0.03\text{ mm}^2\text{sr}$ , which is roughly the same as that of the spectrograph and CCD system. This means that the present lens collection system can be replaced with an optical fiber probe, as is required for *in vivo* operation, with no additional loss in signal.

**[0105]** Figure 19A shows that although the shot noise due to the broadband tissue emission is relatively small, the sloping broadband fluorescence emission still obscures the sharper Raman signals and complicates determination of peak frequencies and identification of weak bands. Furthermore, given the complexity of human tissue, it is likely that this broadband emission will be significant throughout the useful range of the CCD. Any quantitative analysis of the Raman bands in Figure 19A requires that this broadband emission be first removed from the spectrum. The standard methods of removing fluorescence emission from Raman spectra utilize mathematical filters, which rely upon the fluorescence emission being relatively featureless. In an alternative method the excitation frequency is varied over a narrow range (10 - 30  $\text{cm}^{-1}$ ). The Raman band positions vary directly with the excitation frequency, while the fluorescence emission remains fairly constant with such small changes in excitation frequency, allowing it to be efficiently subtracted out. In contrast with mathematical filters, this operation requires no assumptions about the emission lineshape.

**[0106]** To implement this method, the Raman spectrum of the normal aorta specimen is recorded with excitation wavelengths of 810 nm (Figure 19A) and 812 nm. The Raman bands shift with the excitation frequency by 30  $\text{cm}^{-1}$ , while the fluorescence emission remains fairly constant. By subtracting these two spectra, the broadband emission is greatly reduced, and the Raman bands are more readily observed (Figure 19B). This operation is mathematically analogous to taking the derivative of the Raman spectrum, so that the original Raman spectrum can be recovered by integrating the difference spectrum, as shown in Figure 19C. The fluorescence background is greatly reduced in Figure 19C as compared with Figure 19A, allowing easier identification of the Raman bands and their peak frequencies. The integration also smooths the Raman spectrum over a bandwidth similar to the excitation frequency shift and causes some linewidth broadening, as is evident from Figure 19C. Note that the accuracy of this method depends upon the high linearity and stability of the CCD array.

**[0107]** The NIR Raman spectrum of an atherosclerotic plaque with a calcified deposit exposed at the surface collected with the spectrograph and CCD system is shown in Figure 20A. In this case, the broadband emission is nearly 10 times greater than that observed in normal aorta (Figure 19A), resulting in increased noise. However, the intense phosphate stretching vibration at 960  $\text{cm}^{-1}$ , due to the calcified salts, is readily identified. This band is sufficiently intense to be observed in real time and was used in aligning the collection optics. Some weaker bands may also be identified, such as the phosphate/carbonate band at 1070  $\text{cm}^{-1}$ , although these are obscured by the large fluorescence background. By subtracting out this fluorescence (Figure 20B), as above, these bands are much more easily distinguished. The Raman spectrum obtained by integrating the difference spectrum is shown in Figure 20C. The broadband emission is reduced by a factor of 50 relative to Raman bands, and several weaker bands are readily observed. This spectrum is remarkably similar to that of Figure 5a which was observed with the FT-Raman system and 1064 nm

**[0108]** As another example of the sensitivity of the spectrograph and CCD system 300, the Raman spectrum of adventitial adipose tissue is shown in Figure 21, which can be compared to the FT-Raman spectrum shown in Figure 5c. The broadband emission is similar to that of normal aorta, while the Raman bands, due mainly to triglycerides in the tissue, are very strong, resulting in an excellent spectral signal-to-noise ratio.

**[0109]** Thus, the spectrograph and CCD system with 810 nm excitation offers a faster alternative to FT-Raman with 1064 nm excitation and which has greater sensitivity. Even in complex mixtures such as human tissue, the level of background emission observed with 810 nm excitation is low enough to observe the Raman signals. This fluorescence emission does not excessively degrade the signal-to-noise ratio. By subtracting two spectra collected at slightly different excitation wavelengths, and then integrating the difference spectrum, this broadband emission is rejected, yielding high quality Raman spectra. Deconvolution techniques can also be used to selectively remove, or reduce, Raman, fluorescence, or noise light components. Improvements such as using a CW laser to increase the incident intensity and a back-thinned CCD having better red response allows Raman spectra to be collected from intact human tissue in under 1 second. Longer excitation wavelengths may reduce the background emission further. Implementation of the spectrograph and CCD system with a high power diode laser and an optical fiber probe will provide a compact, mobile system for rapidly acquiring NIR Raman spectra remotely from human tissues and will provide a powerful tool for *in vivo* clinical applications.

## Claims

1. A spectroscopic diagnostic system comprising:

- a laser light source (207) for emitting radiation;
- optical cable probe means (20a-c) for inserting into a vascular lumen optically coupled to the laser light source (207) to deliver the radiation to a distal end of optical cable means (20a-c); and
- a spectral analyser to receive and detect Raman shifted radiation, characterised in that:
  - the spectral analyser is a spectrograph and CCD system;
  - the laser light source (207) emits radiation in the infrared spectrum at an excitation wavelength of between 750

nm and 1050 nm;

the optic cable probe means (20a-c) includes a fibre optic cable to deliver laser radiation to a diagnostic site within the vascular lumen and to collect the Raman shifted radiation from tissue or material at the diagnostic site; and

the system includes a programmable control system (215,217) connected to the laser light source (207) and the spectral analyser and is arranged to

a) control delivery of the laser radiation to irradiate a portion of the tissue with a first frequency and then irradiate the same portion of tissue with a second frequency shifted from the first frequency; and

b) detect light emitted by the tissue in response to irradiation by the first frequency to generate a first spectrum of emitted light frequency components, detecting light emitted by the tissue in response to irradiation by the second frequency to generate a second spectrum of emitted light frequency components;

the system further including means arranged to analyse the Raman shifted radiation to permit determination of whether the tissue or material at the diagnostic site is normal vascular tissue or abnormal tissue or material by generating a difference spectrum from the first spectrum and the second spectrum by subtracting one from the other, the difference spectrum containing the Raman shifted frequency components.

2. The spectroscopic system of claim 1 wherein the laser light source (207) is arranged to deliver radiation having first and second irradiation frequencies with a first wavelength of between 750 nm and 900 nm, and the second frequency is shifted from the first frequency by less than  $50\text{ cm}^{-1}$ .

3. The spectroscopic system of claim 1 or 2 further comprising an ablation laser (225) suitable for removing selected tissue from a site.

4. The spectroscopic system of any one of claims 1 to 3, wherein the spectral analyser comprises a filter (62) positioned between the tissue and the detector to optically filter radiation from the tissue.

5. A method of spectroscopic analysis comprising:

irradiating a portion of a biological sample of a vascular lumen to be diagnosed with laser radiation from a laser light source detecting light emitted by the portion of the sample in response to the radiation with a detector, the light having a Raman shifted frequency different from the irradiating frequency; and analysing the detected light to determine a condition of the portion of the biological sample; characterised in that:

the laser radiation has a frequency within the infrared range and an excitation wavelength of between 750 nm and 1050 nm;

the detector comprises a spectrograph and CCD system;

the laser light source (207) and the detector are controlled by a programmable control system arranged to control the delivery of the laser radiation onto the biological sample and the receipt of data from the detector via a fibre optic cable;

the method including the step of analysing the data from the detected Raman shifted frequency;

the irradiating step further comprising irradiating a portion of the tissue with a first frequency and then irradiating the same portion of tissue with a second frequency shifted from the first frequency; and

the detecting step further comprising detecting light emitted by the tissue in response to irradiation by the first frequency to generate a first spectrum of emitted light frequency components, detecting light emitted by the tissue in response to irradiation by the second frequency to generate a second spectrum of emitted light frequency components, and generating a difference spectrum from the first spectrum and the second spectrum by subtracting one from the other, the difference spectrum containing the Raman shifted frequency components,

6. The method of spectroscopic analysis of claim 5 further comprising coupling radiation from a radiation source to a fibre optic cable to transmit the radiation onto the portion of tissue, the fibre optic cable e.g. comprising a catheter for insertion into body lumens, and preferably the fibre optic cable receives light emitted by the tissue and transmits the emitted light to the spectroscope, and, for example, further comprising inserting the catheter into the vascular system.

7. The method of spectroscopic analysis of claim 5 wherein the first and second irradiation frequencies have wave-

lengths of between 750 nm and 900 nm, and the second frequency is shifted from the first frequency by less than  $50 \text{ cm}^{-1}$ .

8. The method of spectroscopic analysis of claim 5 wherein the detecting step further comprises generating the first spectrum and the second spectrum of the emitted light frequency components with the spectroscope and detecting the first spectrum and the second spectrum with the charge coupled device.
9. The method of spectroscopic analysis of claim 8 wherein the spectroscope comprises a single stage spectroscope.
10. The method of spectroscopic analysis of claim 8 wherein the difference spectrum is electronically generated from the first and second spectra detected with the charge coupled device.

## Patentansprüche

1. Spektroskopisches Diagnosesystem aufweisend:

eine Laserlichtquelle (207) zum Emittieren von Strahlung  
einer Optokabel-Sondeneinrichtung (20a-c) zum Einführen in ein Gefäßlumen, die optisch mit der Laserlicht-  
quelle (207) verbunden ist, um die Strahlung an ein distales Ende der Optokabel-Sondeneinrichtung (20a-c)  
zu liefern; und  
einem Spektralanalysator zum Empfangen und Detektieren von Raman-verschobener Strahlung,  
dadurch gekennzeichnet, daß:  
der Spektralanalysator ein Spektrograph und ein CCD-System ist;  
die Laserlichtquelle (207) Strahlung in dem infraroten Spektrum bei einer Anregungswellenlänge zwischen  
750 nm und 1050 nm emittiert;  
die Optokabel-Sondeneinrichtung (20a-c) ein faseroptisches Kabel enthält, um Laserstrahlung an eine Dia-  
gnosestelle innerhalb des Gefäßlumens zu liefern und die Raman-verschobene Strahlung aus dem Gewebe  
oder Material an der Diagnosestelle zu sammeln; und  
das System ein programmierbares Steuerungssystem (215, 217) enthält, das mit der Laserlichtquelle (207)  
und dem Spektralanalysator verbunden und dafür eingerichtet ist:

- a) die Lieferung der Laserstrahlung zum Bestrahlen eines Abschnittes des Gewebes mit einer ersten Fre-  
quenz zu steuern und dann denselben Abschnitt des Gewebes mit einer von der ersten Frequenz verscho-  
benen zweiten Frequenz zu bestrahlen; und
- b) Licht zu detektieren, das von dem Gewebe als Reaktion auf die Bestrahlung mit der ersten Frequenz  
emittiert wird, um ein erstes Spektrum emittierter Lichtfrequenzkomponenten zu erzeugen, Licht zu detek-  
tieren, das von dem Gewebe als Reaktion auf die Bestrahlung mit der zweiten Frequenz emittiert wird, um  
ein zweites Spektrum emittierter Lichtfrequenzkomponenten zu erzeugen;

wobei das System ferner eine Einrichtung enthält, die dafür eingerichtet ist, die Raman-verschobene Strahlung  
zu analysieren, um die Feststellung zu ermöglichen, ob das Gewebe oder Material an der Diagnosestelle nor-  
males Gefäßgewebe oder anormales Gewebe oder Material ist, indem ein Differenzspektrum aus dem ersten  
Spektrum und dem zweiten Spektrum durch Subtraktion voneinander erzeugt wird, wobei das Differenzspek-  
trum die Raman-verschobenen Frequenzkomponenten enthält.

2. Spektroskopisches System nach Anspruch 1, wobei die Laserlichtquelle (207) dafür eingerichtet ist, Strahlung mit  
ersten und zweiten Bestrahlungsfrequenzen mit einer ersten Wellenlänge zwischen 750 nm und 900 nm zu liefern,  
und die zweite Frequenz von der ersten Frequenz um weniger als  $50 \text{ cm}^{-1}$  verschoben ist.
3. Spektroskopisches System nach Anspruch 1 oder 2, welches ferner einen Abtragslaser (225) aufweist, der für die  
Entfernung von ausgewähltem Gewebe von einer Stelle geeignet ist.
4. Spektroskopisches System nach einem der Ansprüche 1 bis 3, wobei der Spektralanalysator ein Filter (62) auf-  
weist, das zwischen dem Gewebe und dem Detektor angeordnet ist, um Strahlung aus dem Gewebe optisch zu  
filtern.
5. Spektroskopisches Analyseverfahren mit den Schritten: Bestrahlen eines Abschnittes einer biologischen Probe  
eines Gefäßlumens, die mittels Laserstrahlung aus einer Laserlichtquelle zu untersuchen ist, indem Licht, das von

dem Abschnitt der Probe als Reaktion auf die Bestrahlung emittiert wird, mittels eines Detektors detektiert wird, wobei das Licht eine von der Bestrahlungsfrequenz unterschiedliche Raman-verschobene Frequenz aufweist; und

Analysieren des detektierten Lichts, um einen Zustand des Abschnittes der biologischen Probe festzustellen; dadurch gekennzeichnet, daß:

die Laserstrahlung eine Frequenz innerhalb des Infrarotbereichs und eine Anregungswellenlänge zwischen 750 und 1050 nm aufweist;

der Detektor einen Spektrographen und ein CCD-System aufweist;

die Laserlichtquelle (207) und der Detektor von einem programmierbaren Steuerungssystem gesteuert werden, das dafür eingerichtet ist, die Lieferung der Laserstrahlung auf die biologische Probe und den Empfang von Daten aus dem Detektor über ein faseroptisches Kabel zu steuern;

wobei das Verfahren ferner den Schritt der Analyse der Daten aus der Raman-verschobenen Frequenz enthält; der Bestrahlungsschritt ferner die Bestrahlung eines Abschnittes des Gewebes mit einer ersten Frequenz und dann die Bestrahlung desselben Abschnittes mit einer von der ersten Frequenz verschobenen zweiten Frequenz umfaßt; und

der Detektionsschritt ferner die Detektion von Licht, das von dem Gewebe als Reaktion auf die Bestrahlung mit der ersten Frequenz emittiert wird, um ein erstes Spektrum emittierter Lichtfrequenzkomponenten zu erzeugen, die Detektion von Licht, das von dem Gewebe als Reaktion auf die Bestrahlung mit der zweiten Frequenz emittiert wird, um ein zweites Spektrum emittierter Lichtfrequenzkomponenten zu erzeugen, und das Erzeugen eines Differenzspektrums aus dem ersten Spektrum und dem zweiten Spektrum durch Subtraktion voneinander umfaßt, wobei das Differenzspektrum die Raman-verschobenen Frequenzkomponenten enthält.

6. Spektroskopisches Analyseverfahren nach Anspruch 5, welches ferner die Einkopplung einer Strahlung aus einer Strahlungsquelle in ein faseroptisches Kabel umfaßt, um die Strahlung auf den Abschnitt des Gewebes zu übertragen, wobei das faseroptische Kabel z.B. einen Katheter zum Einführen in Körperlumina umfaßt, und das faseroptische Kabel bevorzugt von dem Gewebe emittiertes Licht empfängt und das emittierte Licht an das Spektroskop überträgt, und beispielsweise ferner das Einführen des Katheters in das Gefäßsystem mit umfaßt.

7. Spektroskopisches Analyseverfahren nach Anspruch 5, wobei die ersten und zweiten Bestrahlungsfrequenzen Wellenlängen zwischen 750 nm und 900 nm aufweisen und die zweite Frequenz von der ersten Frequenz um weniger als  $50 \text{ cm}^{-1}$  verschoben ist.

8. Spektroskopisches Analyseverfahren nach Anspruch 5, wobei der Detektionsschritt ferner die Erzeugung des ersten Spektrums und des zweiten Spektrums der emittierten Frequenzkomponenten mit dem Spektroskop und die Detektion des ersten und zweiten Spektrums mit der ladungsgekoppelten Vorrichtung umfaßt.

9. Spektroskopisches Analyseverfahren nach Anspruch 8, wobei das Spektroskop ein einstufiges Spektroskop aufweist.

10. Spektroskopisches Analyseverfahren nach Anspruch 8, wobei das Differenzspektrum elektronisch aus dem mit der ladungsgekoppelten Vorrichtung detektierten ersten und zweiten Spektrum erzeugt wird.

## Revendications

1. Système de diagnostic spectroscopique comprenant :

- une source de lumière laser (207) pour émission de radiation, des moyens formant sonde à câble optique (20a-c) pour l'insertion à l'intérieur d'une lumière vasculaire, optiquement couplés à la source de lumière laser (207) pour délivrer la radiation à une extrémité distale des moyens du câble optique (20a-c) ; et
- un analyseur spectral pour recevoir et détecter la radiation décalée, caractérisé en ce que :
  - l'analyseur spectral est un spectrographe et un système CCD ;
  - la source de lumière laser (207) émet des radiations dans le spectre infrarouge à une longueur d'onde d'excitation comprise entre 750 nm et 1050 nm ;
  - les moyens de sonde à câble optique (20a-c) comprennent un câble de fibre optique pour délivrer la radiation laser au site de diagnostic à l'intérieur de la lumière vasculaire et pour collecter la radiation décalée issue du tissu ou du matériel au niveau du site de diagnostic ; et
  - le système comprend un système de contrôle programmable (215, 217) connecté à la source de lumière laser

(207) et l'analyseur spectral et est adapté pour :

- a) contrôler l'émission de la radiation laser de manière à irradier une portion du tissu avec une première fréquence puis irradier la même portion de tissu avec une seconde fréquence décalée de la première fréquence ; et
- b) détecter la lumière émise par le tissu en réponse à l'irradiation par la première fréquence de manière à générer un premier spectre de composantes fréquentielles de la lumière émise, la détection de la lumière émise par le tissu en réponse à l'irradiation par la seconde fréquence pour générer un second spectre de composantes fréquentielles de la lumière émise ;

le système comprenant en outre des moyens appropriés pour analyser les radiations décalées en vue de déterminer si le tissu ou le matériau du site de diagnostic est un tissu vasculaire normal ou un tissu ou matériau anormal, par génération d'un spectre de différence à partir des premier et second spectres en les soustrayant l'un de l'autre, avec le spectre de différence contenant les composantes fréquentielles décalées.

2. Système spectroscopique selon la revendication 1, dans lequel la source de lumière laser (207) est ajustée de manière à émettre des radiations possédant les fréquences des première et seconde irradiations avec une première longueur d'onde comprise entre 750 nm et 900 nm, et la seconde fréquence décalée de la première fréquence d'au moins  $50 \text{ cm}^{-1}$ .

3. Système spectroscopique selon la revendication 1 ou 2 comprenant en outre un laser d'ablation (225) approprié à l'extraction du tissu sélectionné à partir du site à analyser.

4. Système spectroscopique selon l'une quelconque des revendications 1 à 3, caractérisé en ce que l'analyseur spectral comprend un filtre (62) localisé entre le tissu et le détecteur pour filtrer optiquement les radiations issues du tissu.

5. Méthode d'analyse spectroscopique comprenant :

- l'irradiation d'une partie d'un échantillon biologique ou d'une lumière vasculaire à analyser avec une radiation laser issue d'une source de lumière laser, la détection à l'aide d'un détecteur de la lumière émise par la partie de l'échantillon en réponse à la radiation, la lumière ayant une fréquence décalée différente de la fréquence d'irradiation ; et
  - l'analyse de la lumière détectée pour déterminer l'état de la partie de l'échantillon biologique ;
- caractérisée en ce que :
- la radiation laser a une fréquence comprise dans le domaine de l'infrarouge et une longueur d'onde d'excitation comprise entre 750 nm et 1050 nm ;
  - le détecteur comprend un spectrographe et un système CCD ;
  - la source de lumière laser (207) et le détecteur sont contrôlés à l'aide d'un système de contrôle programmable adapté pour contrôler l'émission de la radiation laser sur l'échantillon biologique et la réception des données à partir du détecteur via un câble en fibre optique ;
  - la méthode incluant l'étape d'analyse des données à partir des fréquences décalées détectées ;
  - l'étape d'irradiation comprenant en outre l'irradiation d'une partie du tissu avec une première fréquence puis l'irradiation de la même partie du tissu avec une seconde fréquence décalée par rapport à la première fréquence ; et
  - l'étape de détection comprenant en outre la détection de la lumière émise par le tissu en réponse à l'irradiation par la première fréquence de manière à générer un premier spectre de composantes fréquentielles de la lumière émise, la détection de la lumière émise par le tissu en réponse à l'irradiation par la seconde fréquence de manière à générer un second spectre de composantes de la lumière émise, et la génération d'un spectre de différence à partir des premier et second spectres en les soustrayant l'un de l'autre, le spectre de différence contenant les composantes fréquentielles décalées.

6. Méthode d'analyse spectroscopique selon la revendication 5 comprenant en outre le couplage de la radiation issue d'une source de radiation à un câble en fibre optique pour transmettre la radiation sur la partie du tissu, le câble en fibre optique comprenant par exemple un cathéter pour l'insertion à l'intérieur du corps lumière, et de préférence le câble en fibre optique reçoit de la lumière émise par le tissu et transmet la lumière émise au spectroscopie et, par exemple, comprenant en outre l'insertion du cathéter à l'intérieur du système vasculaire.

7. Méthode d'analyse spectroscopique selon la revendication 5, caractérisée en ce que les première et seconde fréquences d'irradiation ont des longueurs d'onde comprises entre 750 nm et 900 nm, et en ce que la seconde fréquence est décalée de la première fréquence d'au moins  $50 \text{ cm}^{-1}$ .

5 8. Méthode d'analyse spectroscopique selon la revendication 5, caractérisée en ce que l'étape de détection comprend en outre la génération d'un premier spectre et d'un second spectre de composantes fréquentielles de la lumière émise à l'aide du spectroscopie et la détection du premier spectre et du second spectre avec un dispositif à couplage de charge.

10 9. Méthode d'analyse spectroscopique selon la revendication 8, dans laquelle le spectroscopie comprend une étape unique de spectroscopie.

10. Méthode d'analyse spectroscopique selon la revendication 8, caractérisée en ce que le spectre de différence est électriquement généré à partir des premier et second spectres détectés avec le dispositif à couplage de charge.

15

20

25

30

35

40

45

50

55

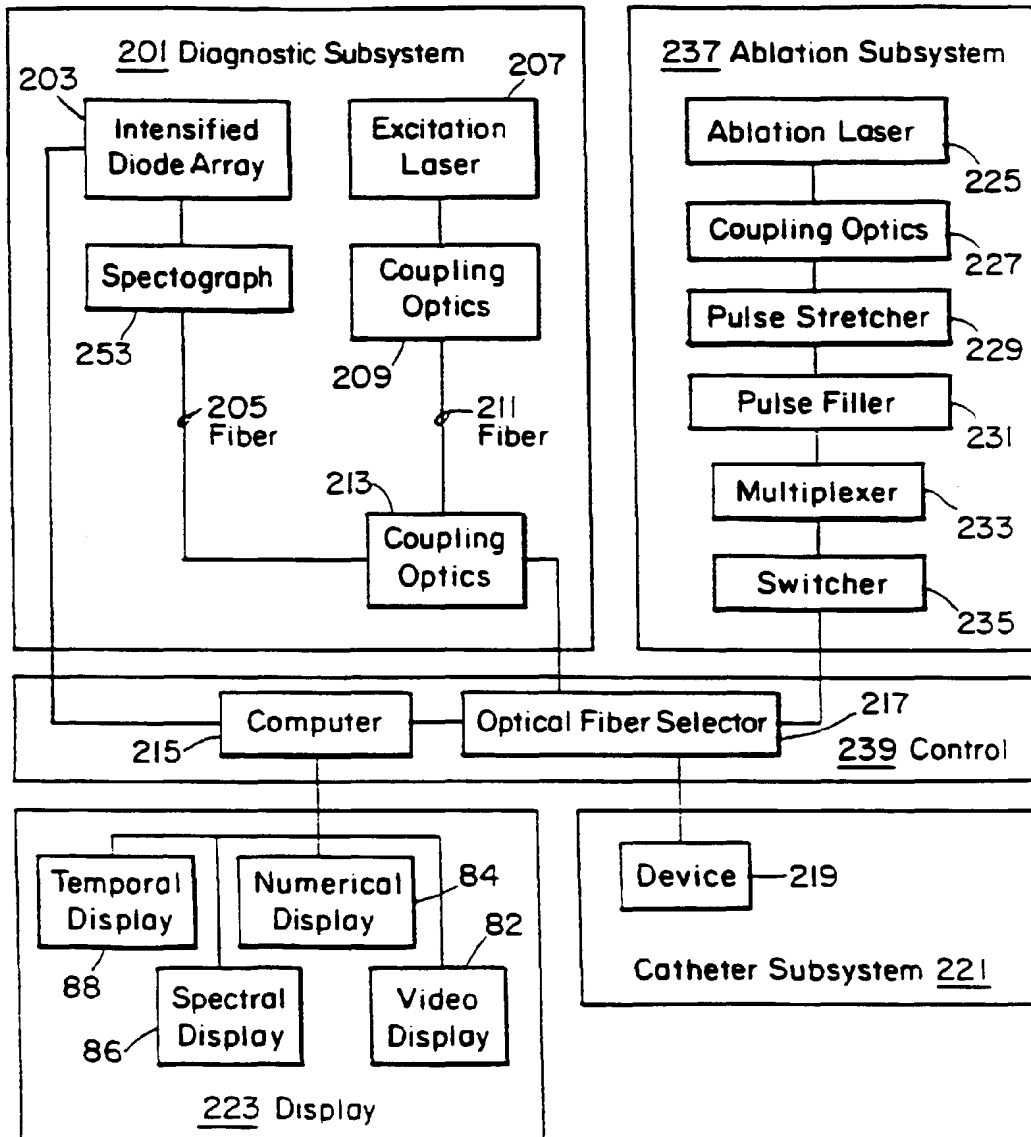


Fig. 1A



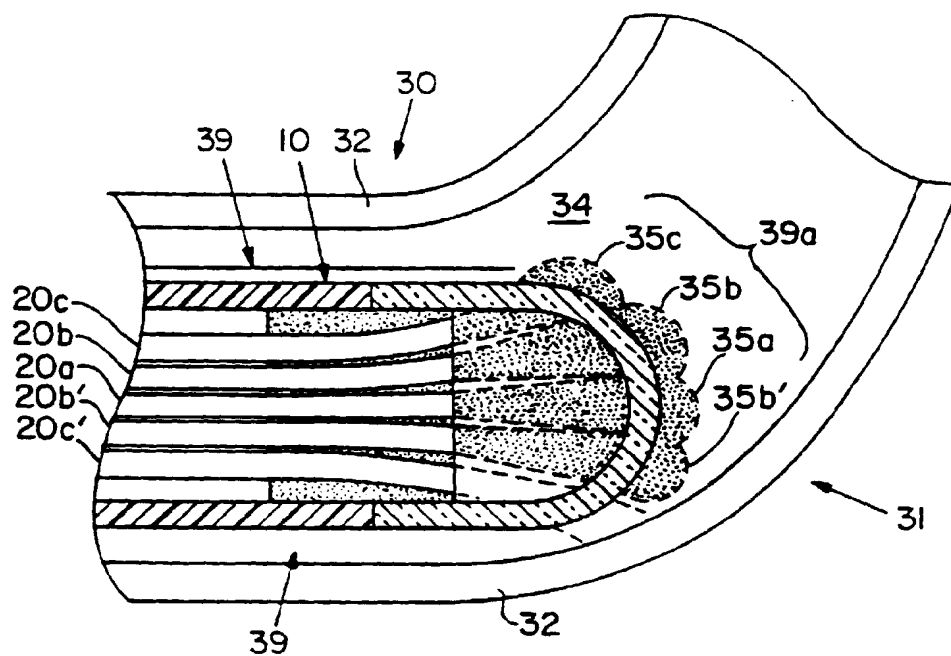


Fig. 1B

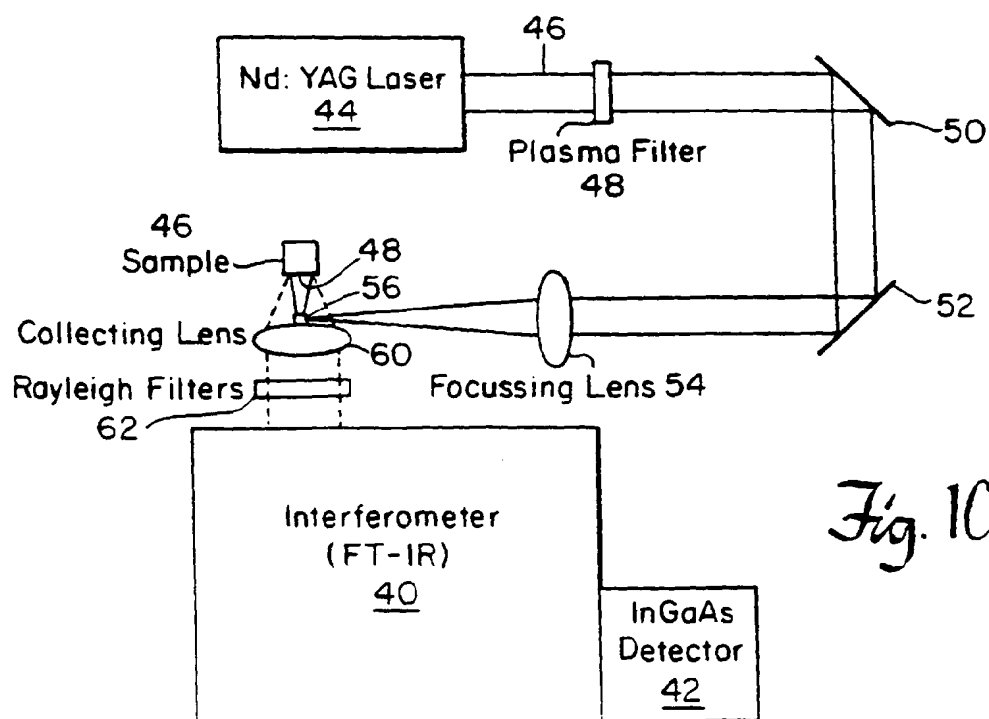
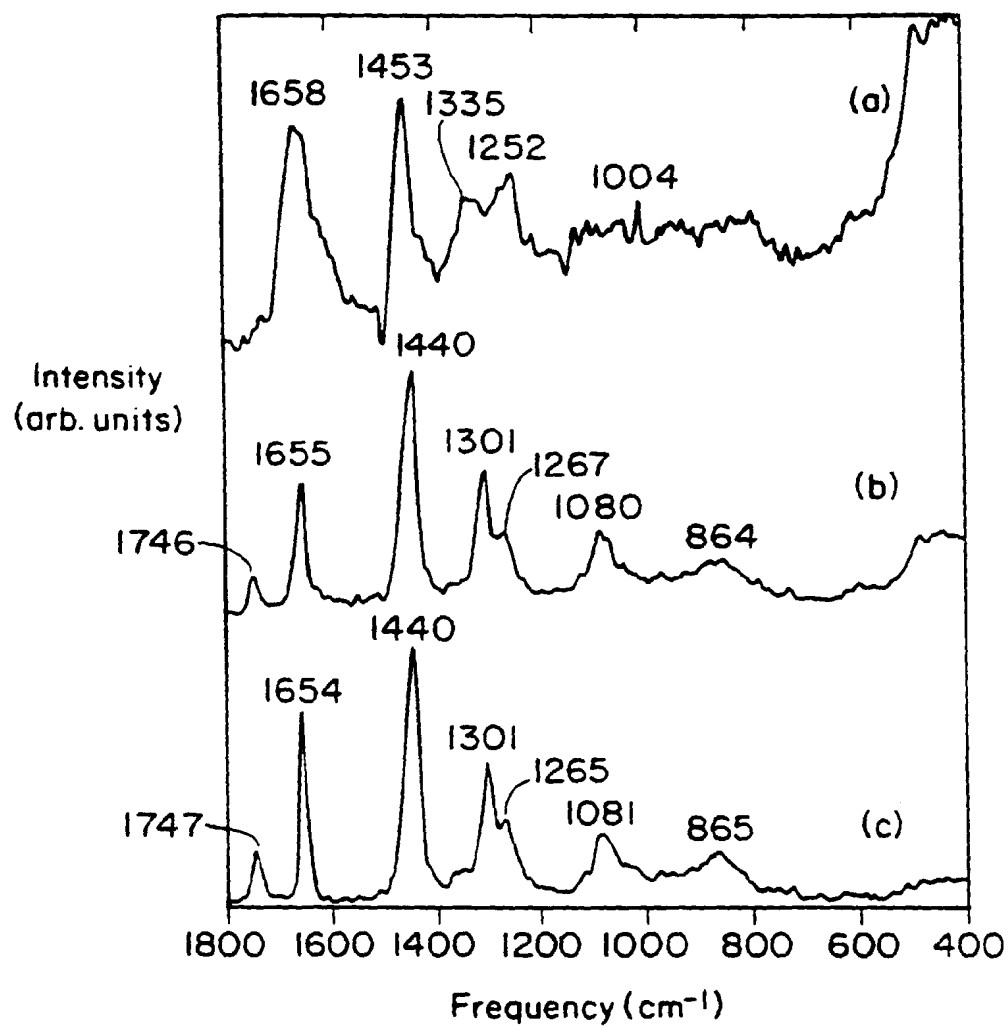
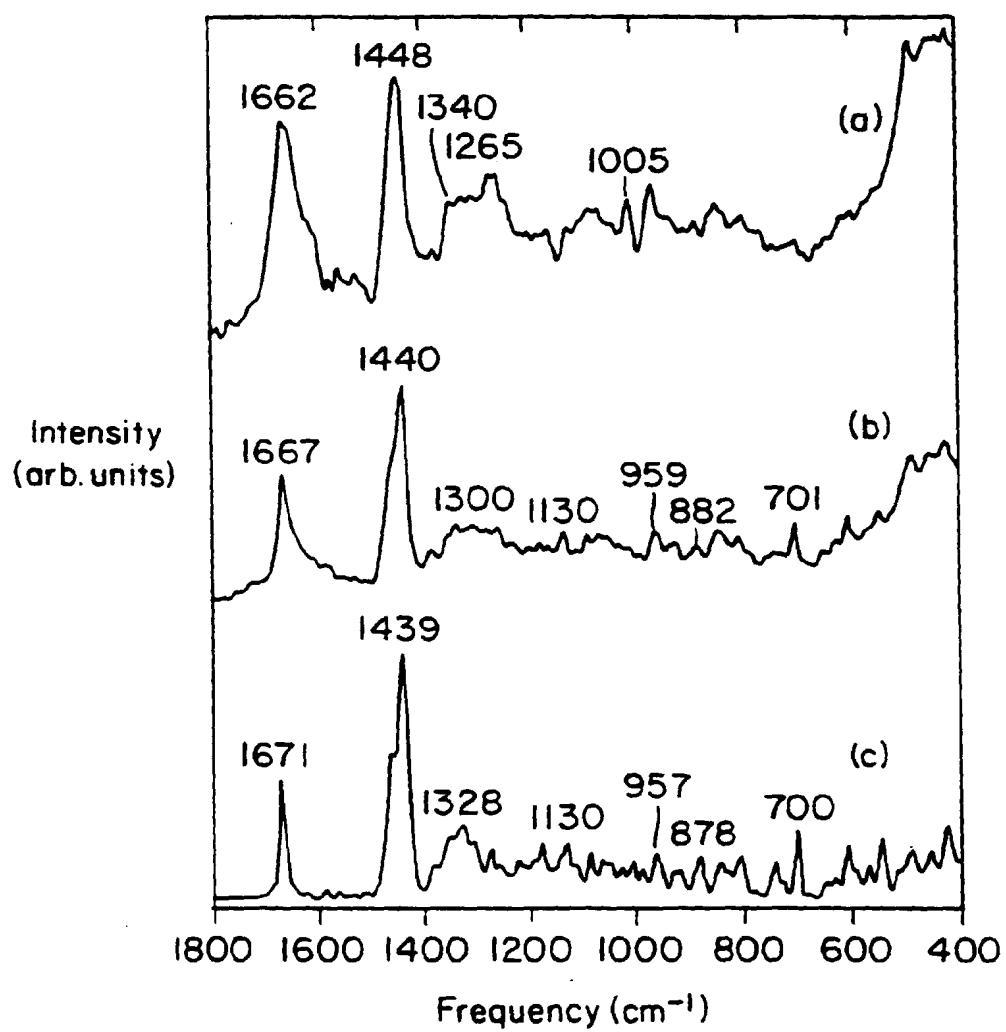
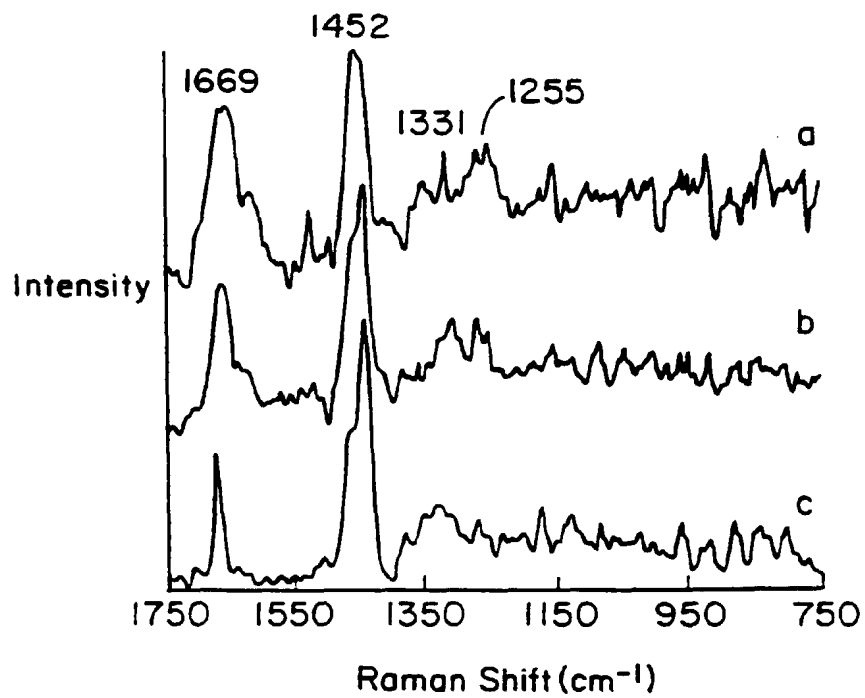
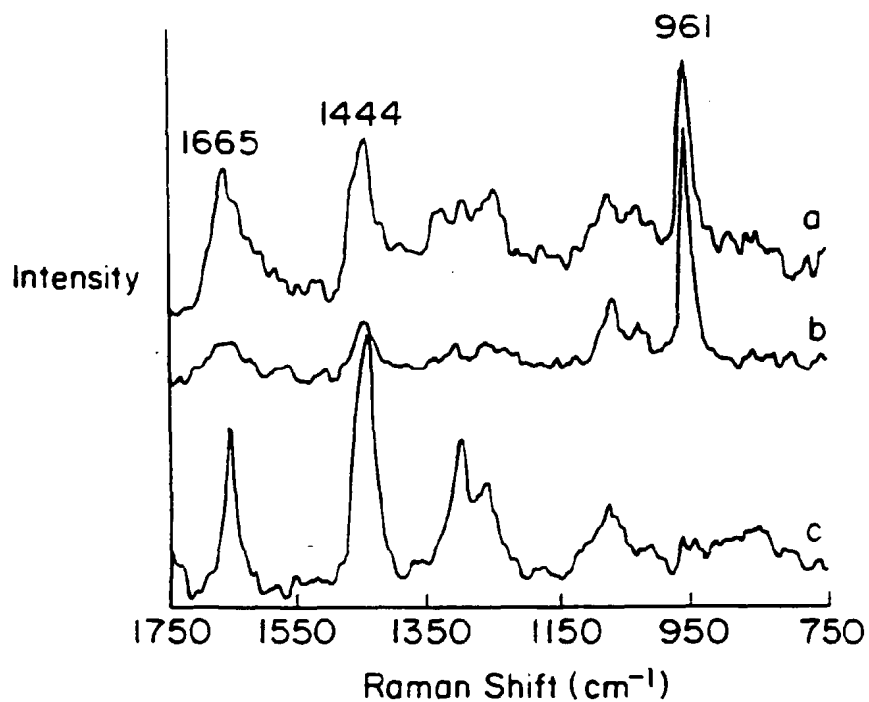
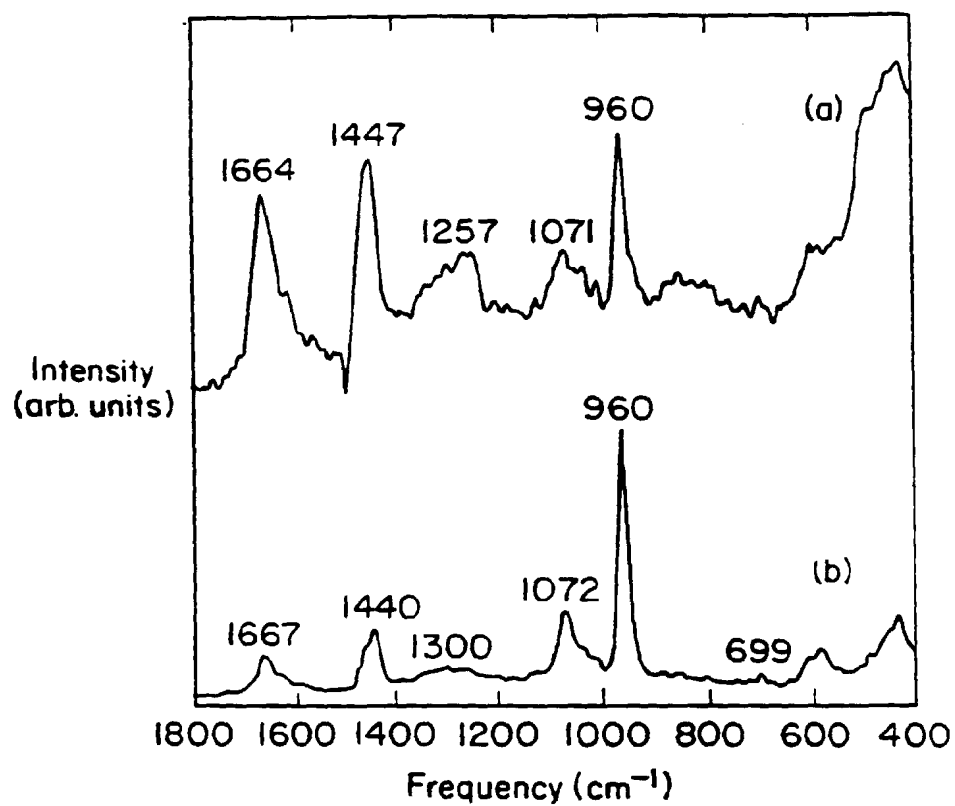
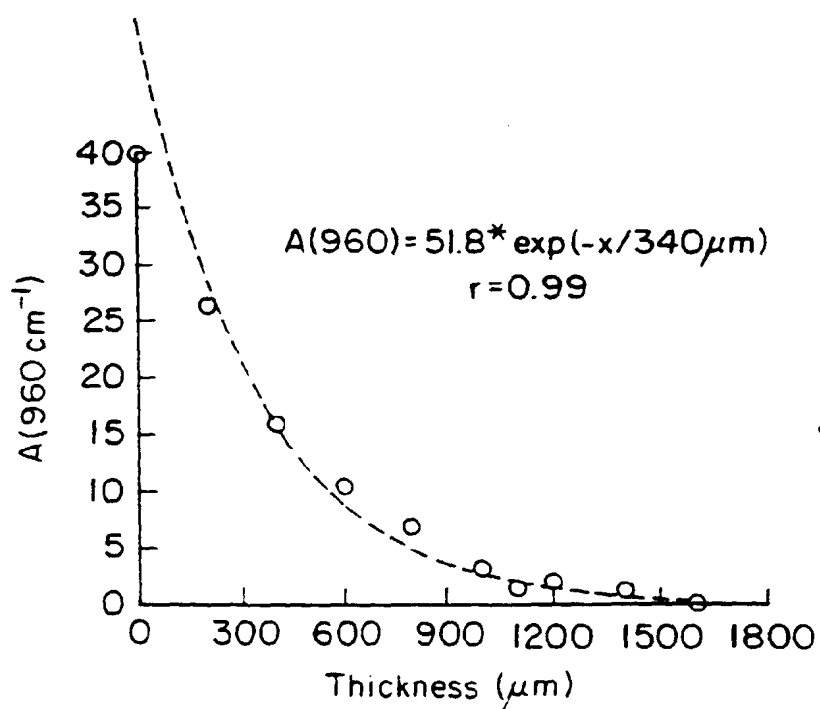


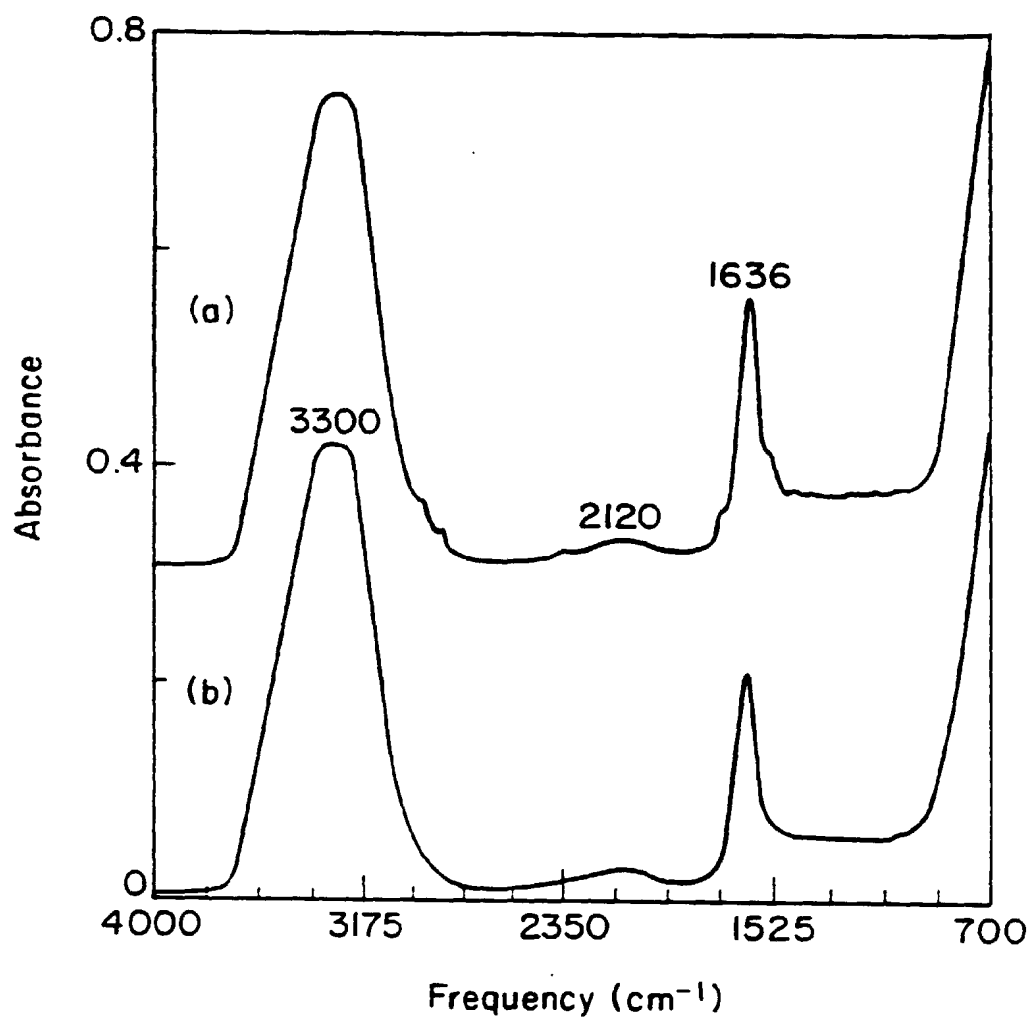
Fig. 1C

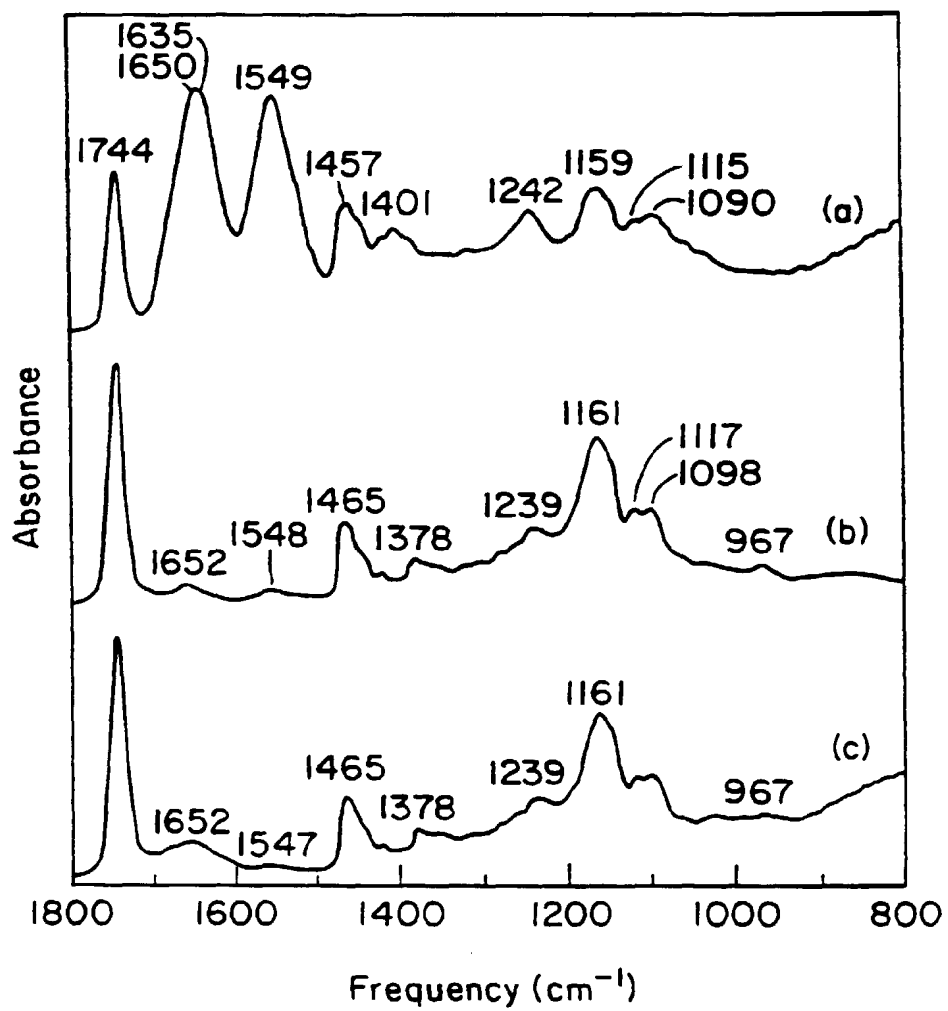
*Fig. 3*

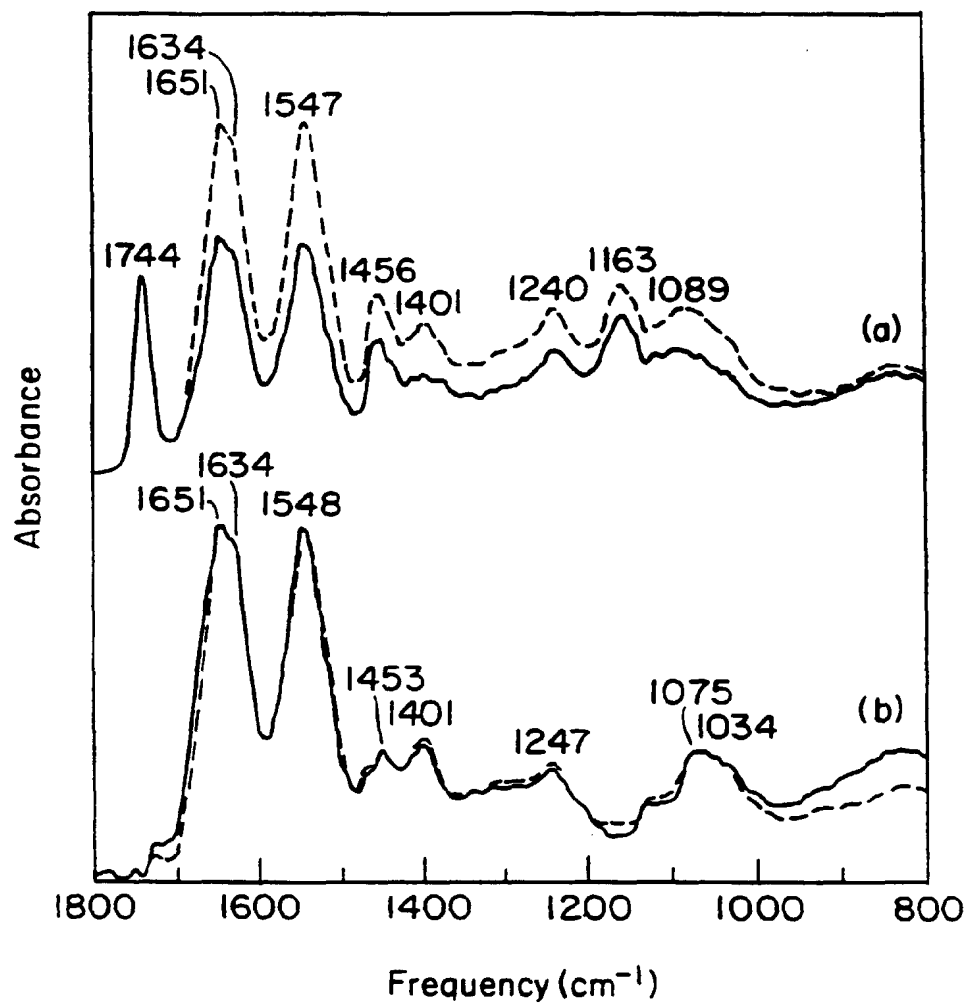
*Fig. 4*

*Fig. 2**Fig. 5*

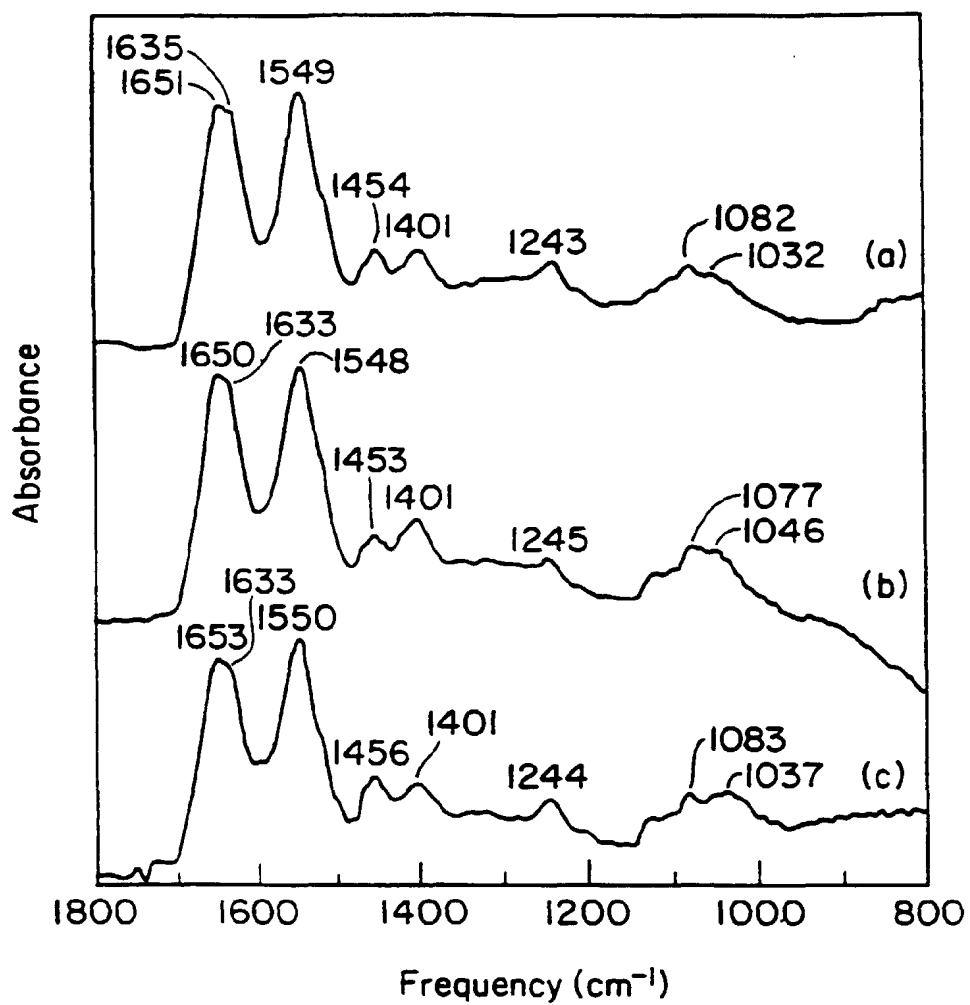
*Fig. 6**Fig. 7*

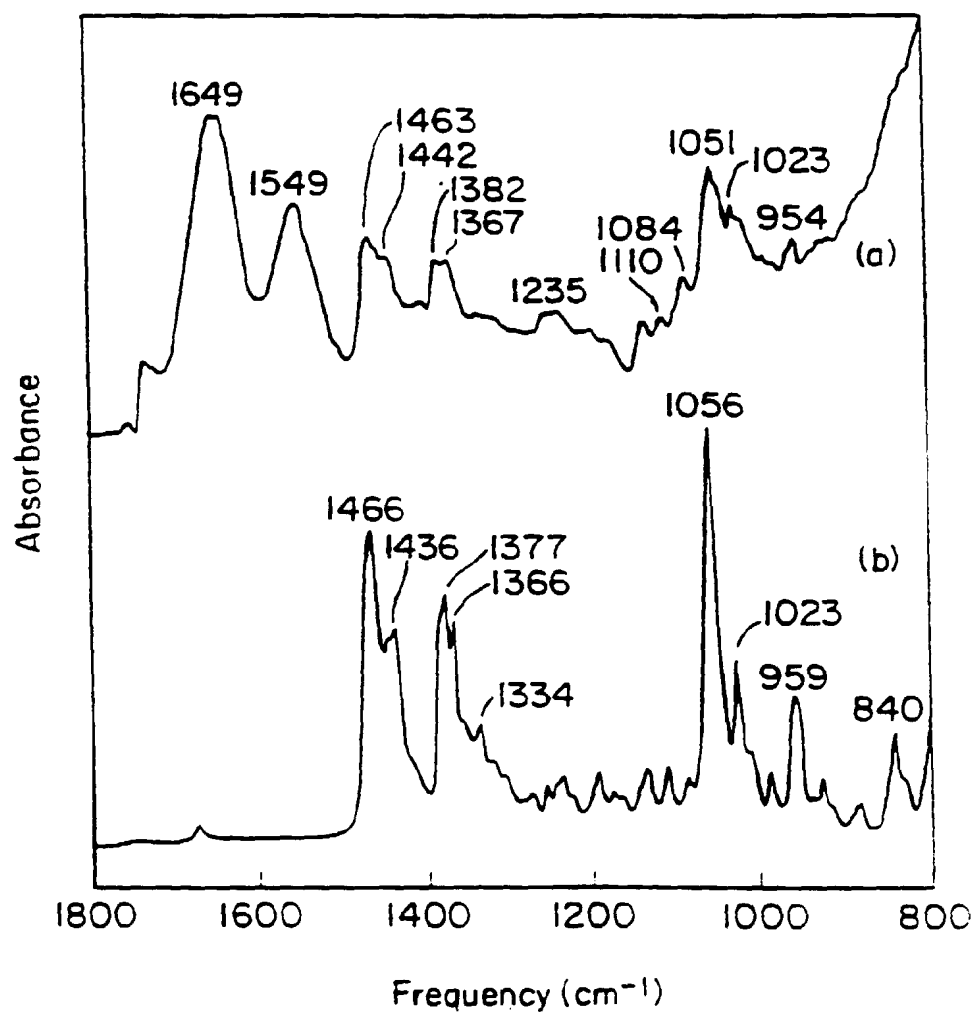
*Fig. 8*

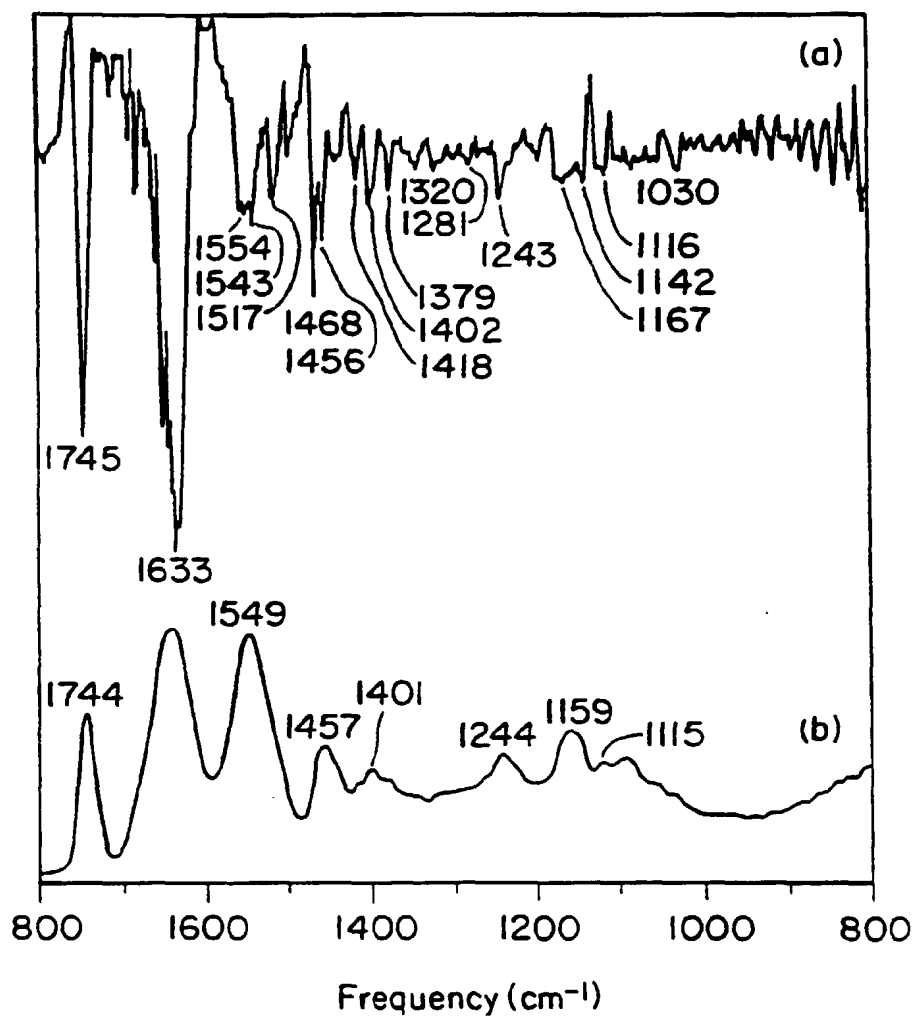
*Fig. 9*

*Fig. 10*



*Fig. 11*

*Fig. 12*

*Fig. 14*

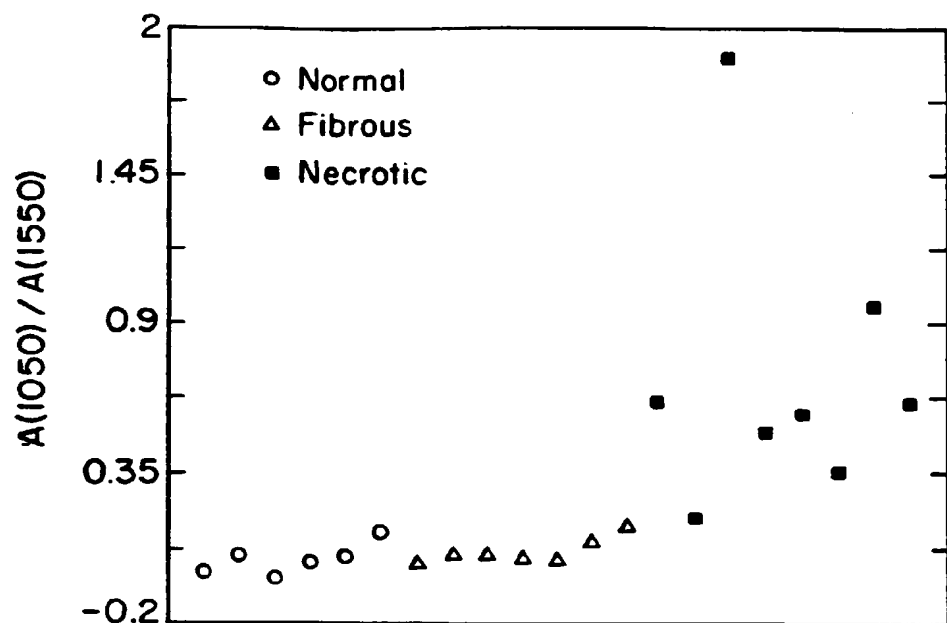


Fig. 13

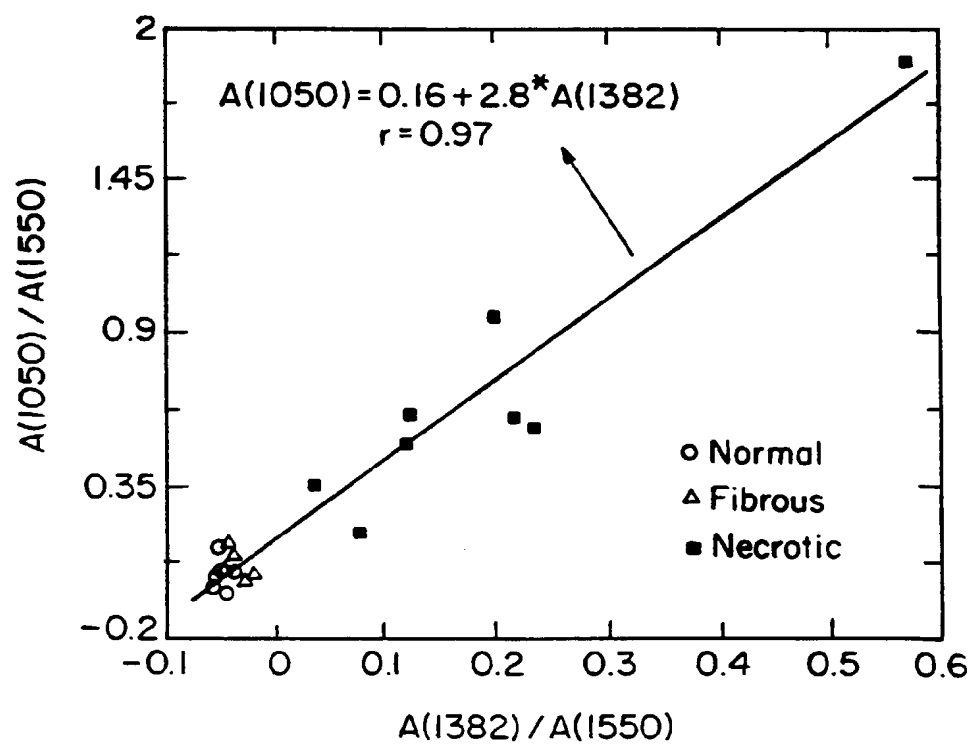
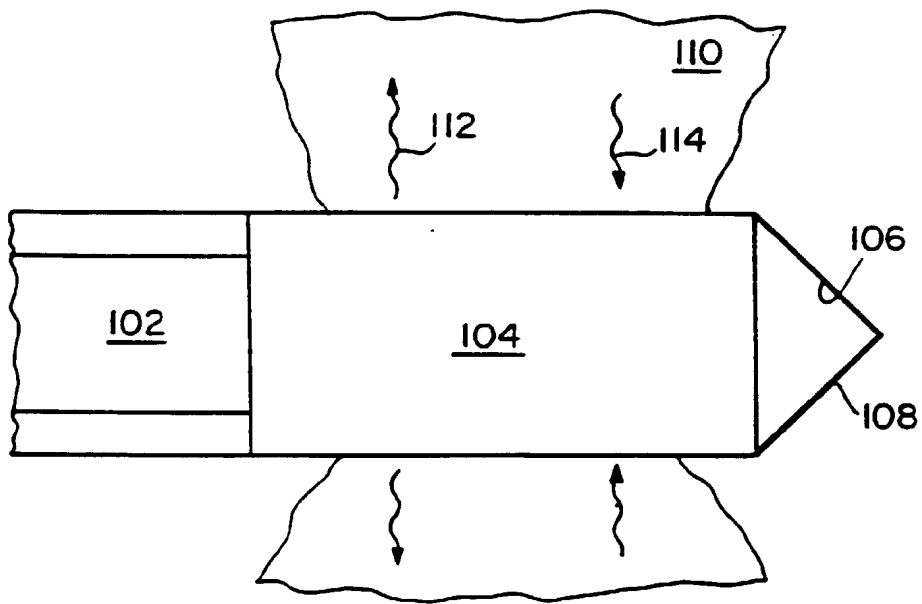
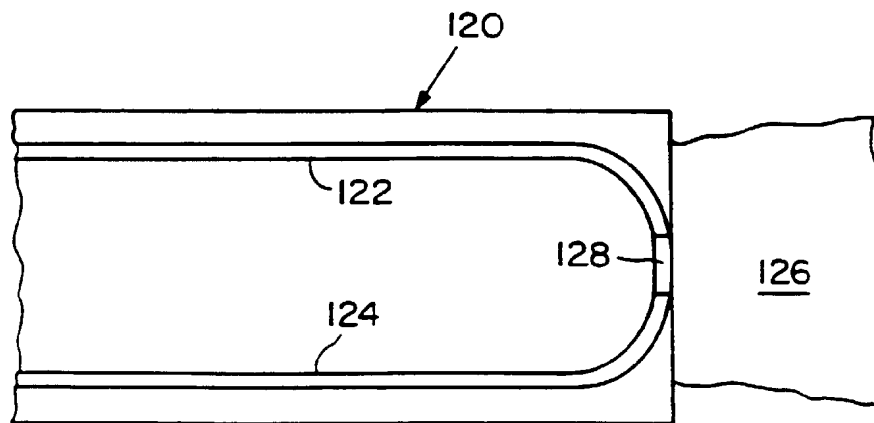


Fig. 15



*Fig. 16A*



*Fig. 16B*

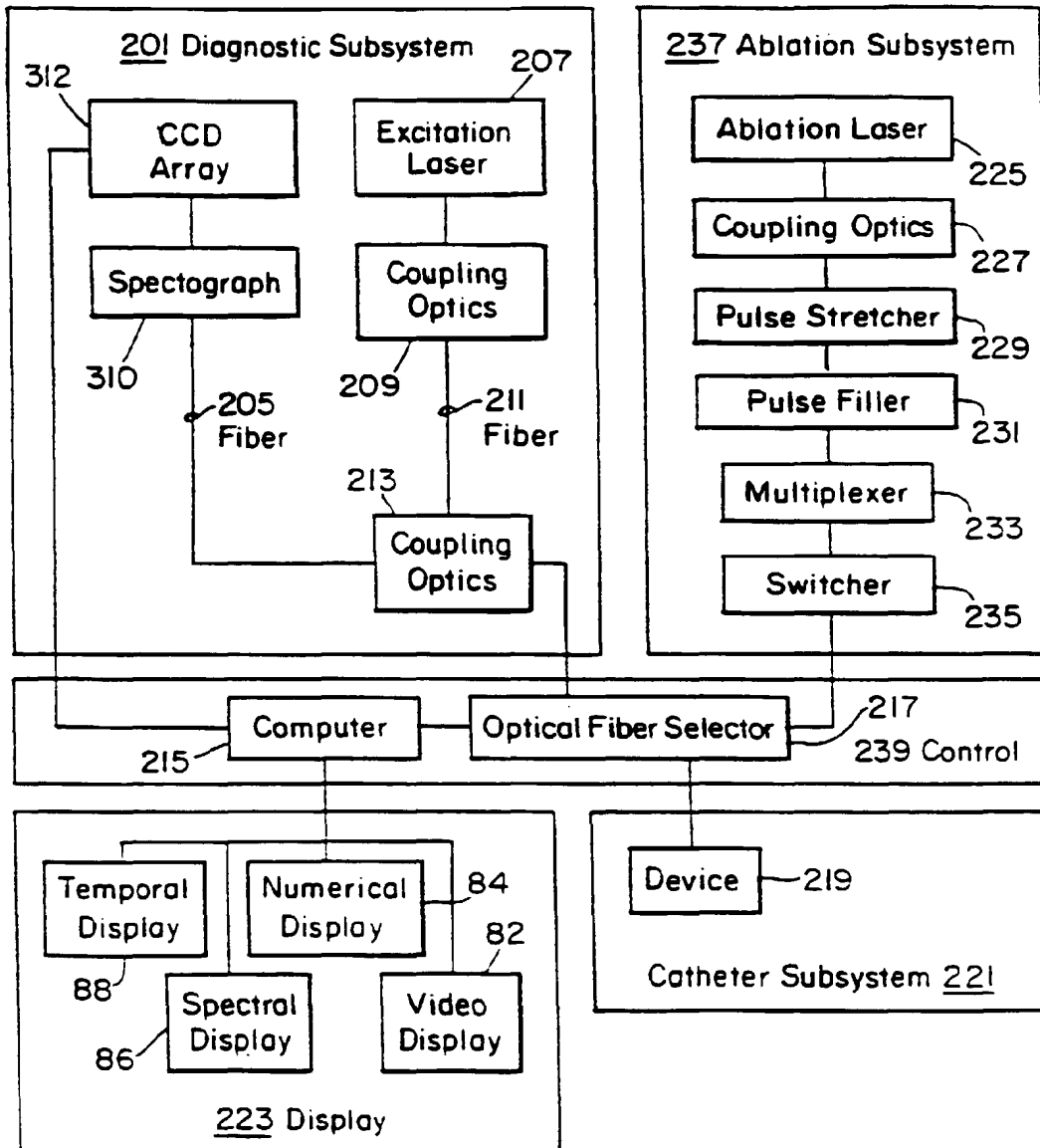


Fig. 17

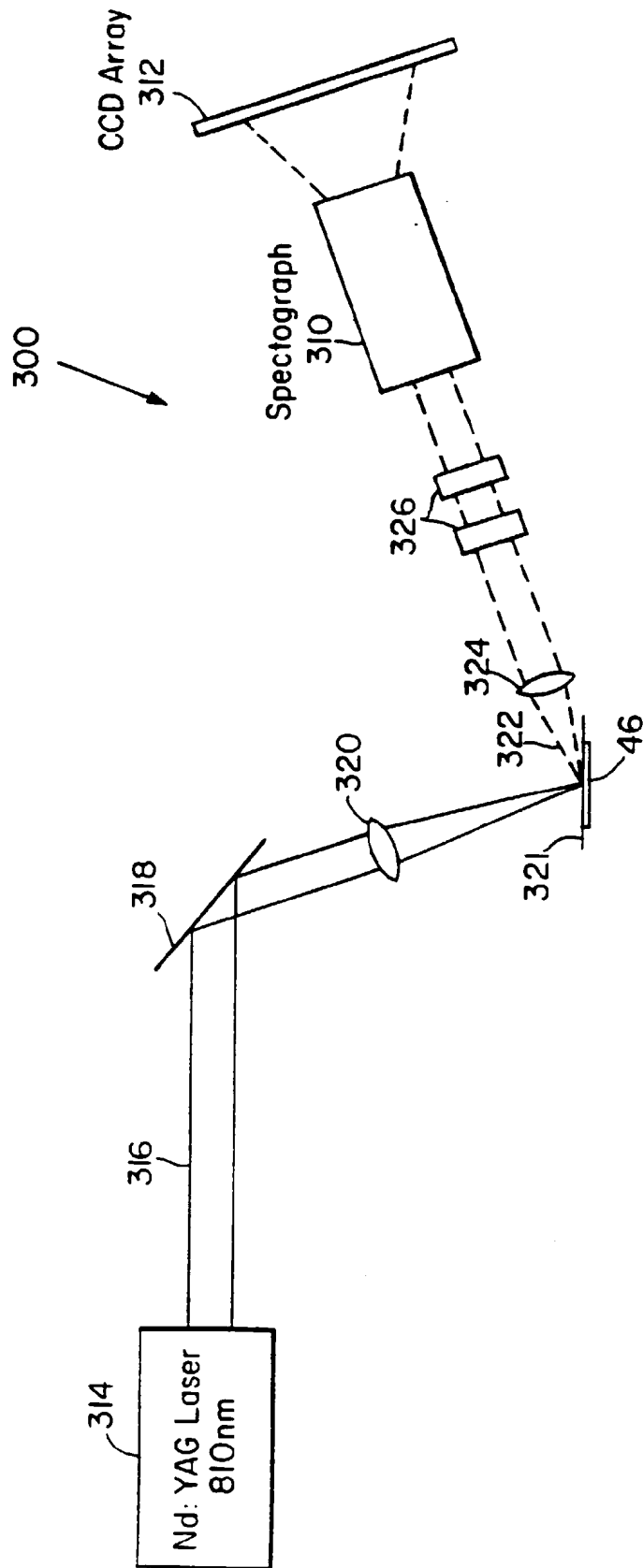
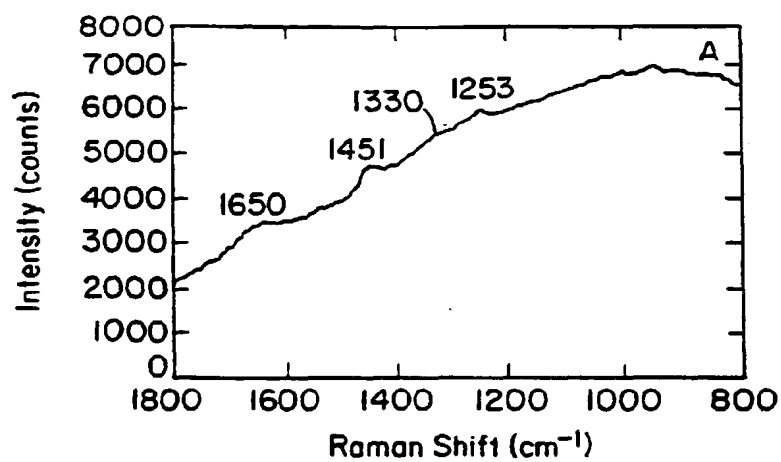
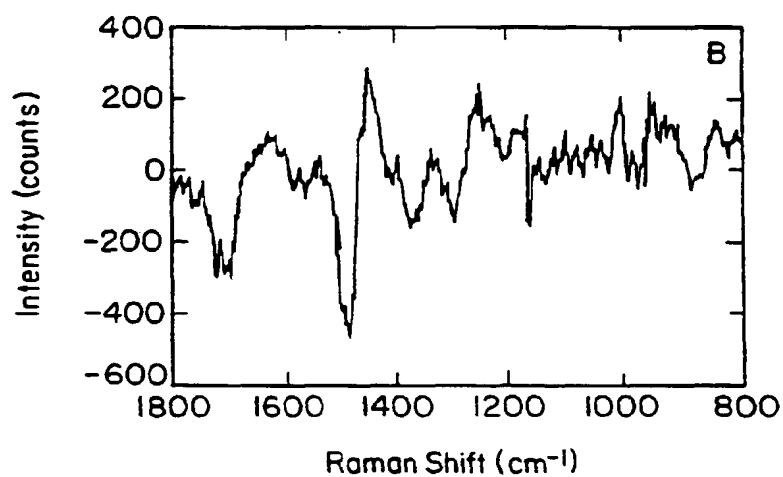
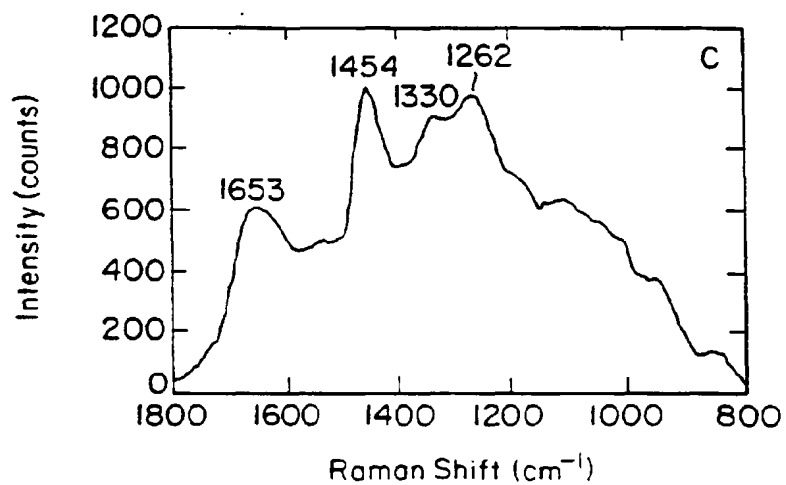
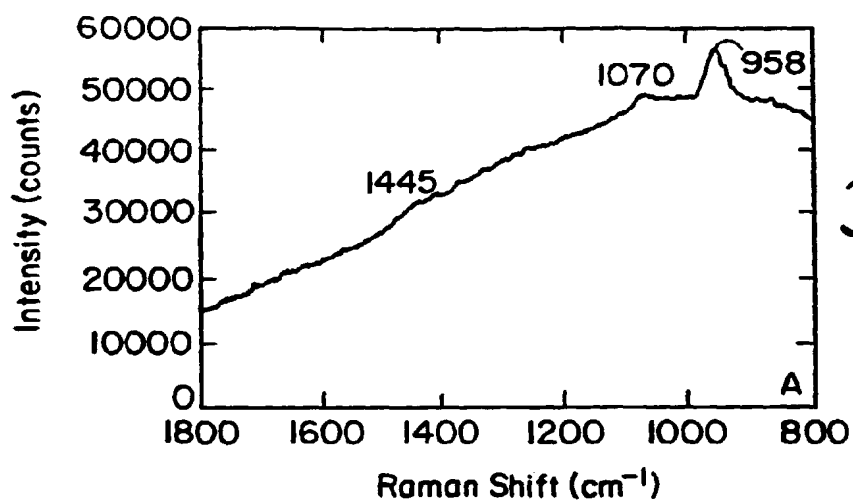
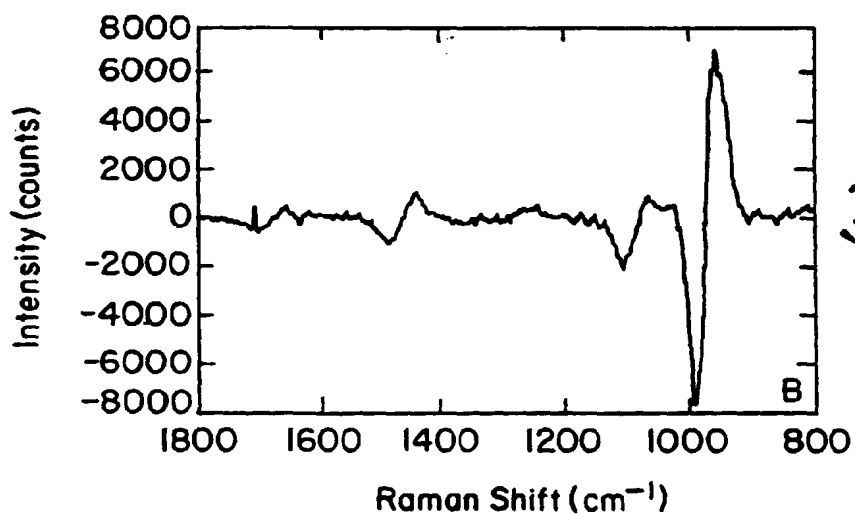
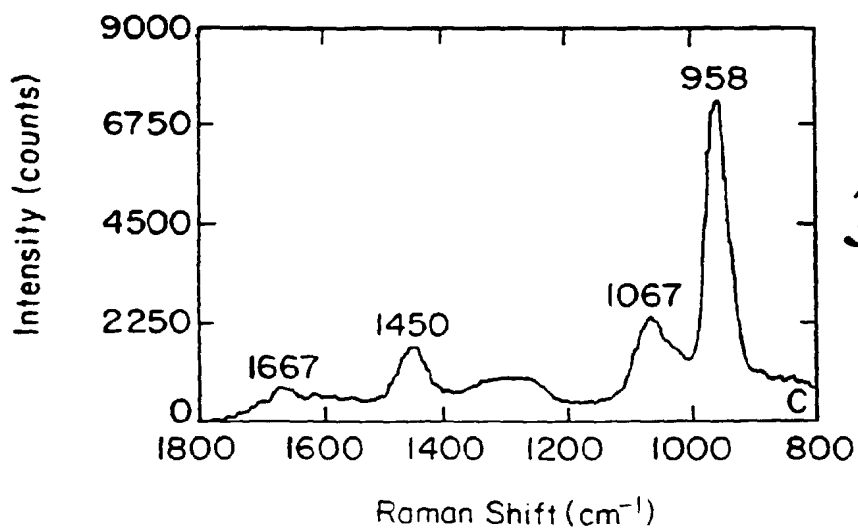
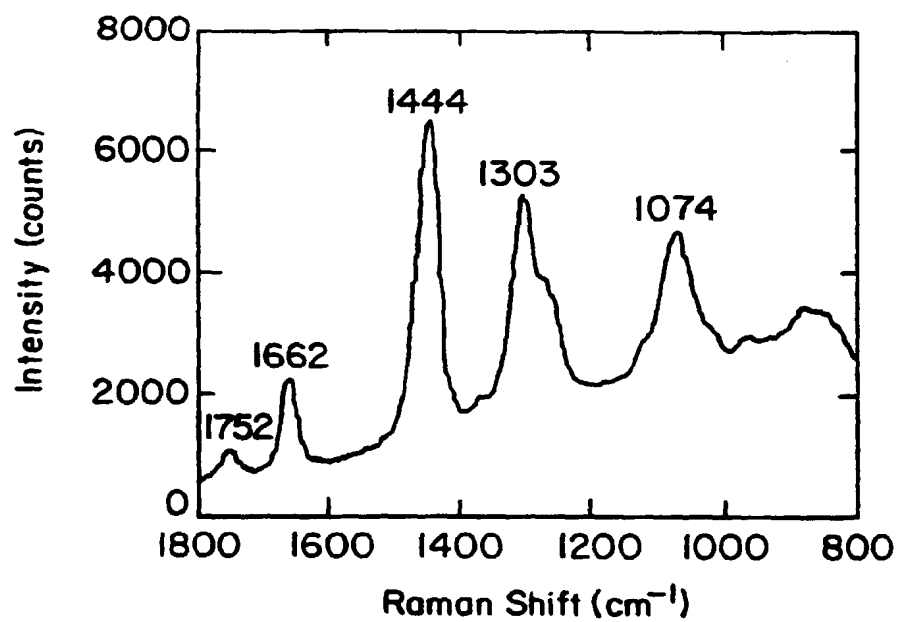


Fig. 18

*Fig. 19(A)**Fig. 19(B)**Fig. 19(C)*



*Fig. 20(A)**Fig. 20(B)**Fig. 20(C)*

*Fig. 21*